An overview on 3D printing of structured porous materials and their applications

Yuanyuan Gao, Jacques Lalevée, Angélique Simon-Masseron

To cite this version:

Yuanyuan Gao, Jacques Lalevée, Angélique Simon-Masseron. An overview on 3D printing of structured porous materials and their applications. Advanced Materials Technologies, In press, 8 (17), ⟨10.1002/admt.202300377⟩. ⟨hal-04133575⟩

HAL Id: hal-04133575
https://hal.science/hal-04133575v1

Submitted on 20 Jun 2023

An overview on 3D printing of structured porous materials and their applications

Yuanyuan Gao[1,2], Jacques Lalevée[1,2*], Angélique Simon-Masseron[1,2*]

[1] Université de Haute-Alsace, CNRS, IS2M UMR 7361, F-68100 Mulhouse, France
[2] Université de Strasbourg, France

*** Corresponding authors:**

Jacques Lalevée, jacques.lalevee@uha.fr

Angélique Simon-Masseron, angelique.simon-masseron@uha.fr

Abstract

Porous materials play an essential role in chemical processes such as catalysis, adsorption, and in emerging technologies for electronic materials, light harvesting and energy transfer. By far, zeolites have contributed most to industrial development. Other porous solid such as activated carbon, metal-organic frameworks (MOFs), covalent organic frameworks (COFs), and porous coordination polymers (PCPs) also have been studied by researchers in the past two decades. The use of porous solids is set to grow in the future, and so is the need to fabricate them into more complex and diverse geometries for a variety of applications. Additive manufacturing, also known as 3D printing has provided the possibility to shape the materials into desired forms, which offers many advantages over their traditional configurations. Structured catalysts, for example, can help to overcome the drawbacks of conventional packed catalyst bed like mass or heat transfer limitations and high pressure drop. This review focus on the latest advances as well as the current challenges in 3D printing of the porous solids. This article aims to contribute to the shape engineering of porous solids and provide a better understanding of their formulations, structures, techniques, properties and applications.

Keywords

Composites, 3D printing, porous materials, zeolites, MOFs

List of abbreviations

ABS	acrylonitrile butadiene styrene
AC	activated carbon
AM	additive manufacturing
BAPO	Phenylbis(2,4,6-trimethylbenzoyl) phosphine oxide
BDMK	2-Benzyl-2(dimethylamino)-4′ -morpholinobutyrophenone
BET	Brunauer–Emmett–Teller
BSA	bovine serum albumin
BTC	benzene-1,3,5-tricarboxylate
BTX	benzene-toluene-xylene
CAD	computer aided design
COF	covalent organic framework
CNTs	carbon nano-tubes
CMC	carboxymethyl cellulose
CV	cyclic voltammetry
DCM	dichloromethane
3DFD	3D fiber deposition
DI	deionized
DIW	direct ink write
DLP	digital light processing
DMDs	digital micromirror devices
DME	methanol to dimethyl either
DMF	dimethylformamide
EDLC	electrochemical double layer capacitor
ESA	electrical swing adsorption
FDM	fused deposition modelling
FFF	fused filament fabrication
GCD	galvanostatic charge/discharge
GMA	glycidyl methacrylate
GO	graphene oxide
HCPK	1-Hydroxycyclohexyl phenyl ketone
HDDA	1,6-hexanediol diacrylate
HEC	hydroxyethyl cellulose
HIM	helium ion microscopy
HNTs	halloysite nanotubes

HPMC	hydroxypropyl methyl-cellulose
LCD	liquid crystal display
LED	light-emitting diode
LPBF	laser powder bed fusion
MB	methylene blue
MC	methylcellulose
MOF	metal organic framework
MMA	methacrylic acid
MTH	methanol to hydrocarbon
MTO	methanol to olefin
NMP	n-methyl-2-pyrrolidone
N/S	not specified
PA	polyamide
PAA	polyacrylic acid
PC	polycarbonate
PCP	pulsed current processing
PCPs	porous coordination polymers
PEI	polyethylenimine
PEGDA	poly(ethylene glycol) diacrylate
PEK	polyetherketone
PI	photoinitiator
PIS	photoinitiating system
PLA	poly(lactic acid)
PPSF	polyphenylsulfone
PVA	polyvinyl alcohol
PVDF-HFP	poly(vinylidene fluoride-co-hexafluoropropylene)
PVOH	polyvinyl alcohol
PVP	polyvinylpyrrolidone
RH	relative humidity
SEM	scanning electron microscopy
SLA	stereolithography
SLM	selective laser melting
SLS	selective laser sintering
STL	standard triangle language/standard tessellation language
TEDGMA	triethylene glycol dimethacrylate
TEOS	tetraethylorthosilicate

TMPTA	trimethylolpropane triacrylate
TMPPTA	trimethylolpropane propoxylate triacrylate
TPD	temperature programmed desorption
TPE	thermoplastic elastomer
TPO	2,4,6-Trimethylbenzoyl diphenylphosphine oxide
TPU	thermoplastic polyurethane
TRGO	thermally reduced graphene oxide
UMDA	urethane dimethacrylate
UV	ultraviolet
XRD	X-ray diffraction

1. Porous solids

Porous materials can be divided into three groups according to their pore size: a) microporous materials where the pore diameter is smaller than 2 nm, b) mesoporous material with pore diameter between 2-50 nm and, c) macroporous materials, which have pores larger than 50 nm. Porous solids are widely recognized for their high surface areas, adsorption capacities, and catalytic properties. The chemical and physical properties of these materials can be tailored to suit specific applications through precise control of their atomic-level structure. This level of control allows for the optimization of properties such as selectivity towards specific molecules, catalytic activity, and thermal stability.[1–3] Characteristics of the various porous solids considered in this review are reported in Table 1.

1.1. Zeolites

Zeolites are the most important heterogeneous catalysts used in industry and have been applied to refining petrochemistry, environmental catalysis and synthesis of fine chemicals. They are a set of crystallized aluminosilicates consisting of a framework based on three-dimensional structure of SiO_4 and AlO_4 tetrahedra molecules linked to each other by sharing oxygen. The presence of aluminum with oxidation state +III in zeolite framework creates negative charges that must be compensated by extra-framework cations which are responsible for the ion exchange properties.[4,5] Additionally, the acidity of zeolites, which is a key factor in determining their catalytic properties, is directly related to the amount of aluminum in the framework.[6] The general formula of zeolite can be written as $M_{2/n}O.Al_2O_3.xSiO_2.yH_2O$, where ‘x’ is always equal to or greater than 2 and ‘n’ is the valence of the extra-framework cation ‘M’.[7] The Si/Al molar ratio varied between 1, in type-A zeolite, and infinite in silicalite for example.[8] More than 250 topologies have been now identified : they differ in pore size (pore diameter < 1 nm), shape (channels/cavities), and their connectivity.[9] These microporous materials offer advantages such as high surface area (ca. 600-700 m^2/g), thermal stability (ca. 700-900°C, depending on the chemical composition), selectivity, and non-toxicity. Therefore, they have a diverse range of applications in various domains as adsorption, gas separation, water treatment, ion exchange, catalysis, medicine and in optics.[10–16]

1.2. MOFs and COFs

Due to the growing interest in molecular design, metal-organic frameworks (MOFs) have been extensively investigated over the past 20 years.[17] These compounds are part of the class of coordination polymers composed of metal ions or clusters coordinated to organic ligands (linkers) for form one-, two-, or three-dimensional structures. Most of the MOFs reported in the literature are crystalline. The periodic coordination polymeric networks are generated during the synthesis, leading to the formation of crystalline materials with very high porosity, large surface area (1000-10000 m^2/g), with highly tunable pore sizes (usually 0-3 nm, up to 9.8 nm).[17] In most cases for MOFs, the pores are stable during the elimination of the guest molecules (often solvents). The chemical properties, pore sizes and the overall surface area can be tailored by using different metal ions and organic molecules as linkers. Thanks to the highly ordered and porous structure, these materials have many potential applications in domains as adsorption, catalysis, bioimaging, and sensing.[18–21] Despite their many attractive properties, MOFs have yet to find widespread industrial or commercial use, mainly due to their high cost, relatively poor thermal and mechanical stability, and limited ability to function in aqueous environments.[22]

Similar to MOFs, covalent-organic frameworks (COFs) are also a class of crystalline porous polymers.[22] The porous organic frameworks form two- or three-dimensional structures through reactions between organic precursors resulting in strong covalent bonds to provide porous and stable materials (up to 600°C). These coordination polymers allow the precise integration of organic units to form predesigned skeletons and nanopores. Pore size ranges from 0.7 to 2.3 nm. Even they are developed less and later than MOFs, the great potential for functional exploration makes them on of the most popular materials investigated in recent years. As COFs are composed of light-weight elements linked by strong covalent bonds, they have low mass densities and provide permanent porosity.[23] These properties make them ideal candidates for gas storage.

1.3. Carbon adsorbents

Activated carbon were treated with a chemical or thermal activation process to get high porosity with micro-, meso- and/or macropores and high specific surface area (between ca. 500 to 1500 m^2/g).[24] They can be produced from most organic resources, but agricultural by-products are most commonly used since they are affordable and sustainable. A carbonization process is required for the carbon materials to control the morphology and pore structure, where randomly oriented graphitic microcrystals and strong cross-linking were built. The well-developed three-dimensional hierarchical porous structure and high reactivity make it a promising adsorbent for many species, especially CO_2. The adsorption capacity of activated carbons at ambient pressure is high. They don't require any moisture removal and are easy to regenerate but their thermal stability depends on the atmosphere (ca. 400°C under air and ca. 800°C with nitrogen).[25] They are commonly used to fix organic pollutants and heavy metals but also as the electrode materials for supercapacitors thanks to its large surface area, good conductivity, and low cost.[26–28] Furthermore, the possibility of modifying surface chemistry with formation of specific surface groups allow a more efficient adsorption.[29]

Table 1. Characteristics of different porous solids with open framework

	Zeolites 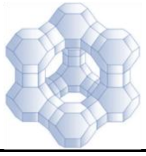	**Metal-organic frameworks** 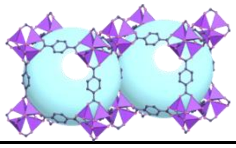	**Covalent-organic frameworks** 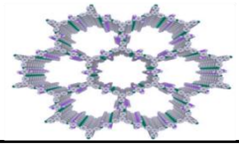	**Carbon adsorbents** 
Crystallinity	Typically high	Low to typically high	High	Amorphous
Porosity	Micropores, narrow pore size distributions	Micro- or mesopores, very high surface area, narrow pore size distributions	Micro- or mesopores, very high surface area, narrow pore size distributions	Micro- to macropores, broader pore size distributions, high surface area
Stability	Good thermal stability, sensitive to strongly acidic/basic media	Poor thermal stability but depends on the structure, mostly unstable in aqueous medium, poor mechanical stability	Poor with boronate ester linkages, good with imine linkages [22,30,31]	Good thermal and chemical stabilities
Main applications	Water adsorption, water treatment, gas separation, petrochemistry, medicine and optical domains	Adsorption, catalysis, bioimaging, and sensing	Biomedicine, sensing, optoelectronics, catalysis, gas storage	Gas storage, electrodes, agriculture, purification, medicine, air filters, skin care
Advantages	Good thermal stability, low cost, commercially proven synthesis technology	Very high diversity of structures	Tunability of electronic properties	Low cost, possibility to modify the surface chemistry, commercially proven synthesis technology
Summary	Well-developed porous materials on an industrial scale in various domains, still growing area of interest	Materials with high potential application, still limited large-scale synthesis	Much less developed area, but great potential for organic electronics	Commercially available; wide applications in industry, porosity controlled by activation process

1.4. The importance of shaping process

The shaping process plays a crucial role in the application of porous materials by transforming the as-synthesized powders or aggregates into objects with desired geometries, such as pellets, beads, or extrudates (Figure 1). By crystallization on/from a support, hollow fibers and monoliths can be designed. Interest in 3D printing object manufacturing continues to grow.

This step is essential as it imparts mechanical strength, structural integrity, and improved handling properties to the porous materials, enabling their efficient use in diverse industries. One of the key reasons for shaping porous materials is to enhance their mass transport properties. The formation of well-defined geometries facilitates the efficient diffusion of gases, liquids, or ions through the material's interconnected pore network. This is particularly critical for applications involving catalysis, gas separation, adsorption, and ion exchange, where the availability of accessible surface area and optimal transport pathways directly impact the performance.

Moreover, shaping also enables the integration of porous materials into existing manufacturing processes or devices. By forming them into specific shapes, these materials can be seamlessly incorporated into reactors, columns, filters, and other equipment, facilitating their industrial implementation and scale-up. The ability to shape porous materials according to the specific requirements of a particular application expands their practical utility and widens the scope of their potential uses.

This review aims to summarize the existing process for porous material shaping achieved through 3D printing technology. In the following sections, we will provide an overview of the conventional shaping methods and different additive manufacturing techniques. Subsequently, the materials that can be structured and their respective applications have been classified according to the different 3D printing technologies. Additionally, the challenges and outlook for each printing method is summarized.

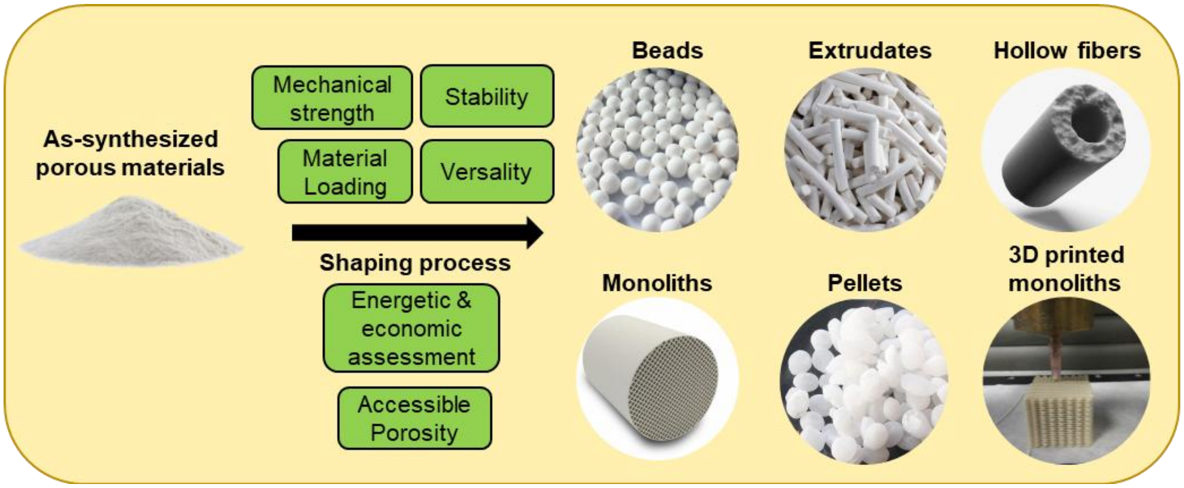

Figure 1. Different shapes for porous materials and characteristics/aspects to be taken into consideration when shaping.

2. Conventional manufacturing approaches

By using a variety of shaping processes, such as extrusion, slip casting, spray drying and granulation, pelletizing, porous powders are transformed into common geometrics like pellets, beads, and extrudates structures as illustrated with some example in Figure 2. The general processing steps can be concluded as follows: (i) mixing the porous powder with inorganic or organic binders, (ii) shaping the powders into the desired engineering shapes, and (iii) removing temporal additives and fabricating objects with robust mechanical properties by thermal treatment. Some organic additives are added in order to facilitate the shaping process (such as temporary binders, dispersants or plasticizers) and can be eliminated by the subsequent thermal treatment, which is primary performed to increase the bonding strength between the solid particles in the shaped body. On the other hand, inorganic binders such as clay and silica are added to reinforce the physical strength by adhesion and cohesion. Several reports have pointed out that zeolite-binder interactions can influence the reactivity, selectivity and stability of the overall material. For example, clay binders can influence the acidity of catalyst and improve coke stability; Al_2O_3 can create additional Brønsted acid sites and influence the product selectivity; SiO_2 may cause dealumination of the zeolite framework and induce a loss of Brønsted acidity.[32] In contrast, binderless processing techniques such as hydrothermal transformation[33] and pulsed currents[34] can minimize the use of inactive binders without compromising mechanical strength.

Adsorbent or catalyst beads are normally produced *via* spray drying (Figure 2a), which is a procedure that converts a solution/suspension into droplets, forming a spray, dried under very hot gas (air or nitrogen) to form beads by evaporation of a solvent. During the atomization process, the fed droplets have a high surface area per unit of weight that allows fast and effective conversion to solid beads. Spray drying is one of the most effective ways for the shaping of different compounds and composites that allows for a remarkable control over final product properties: particle size distribution, residual moisture content, bulk density, and morphology.[35]

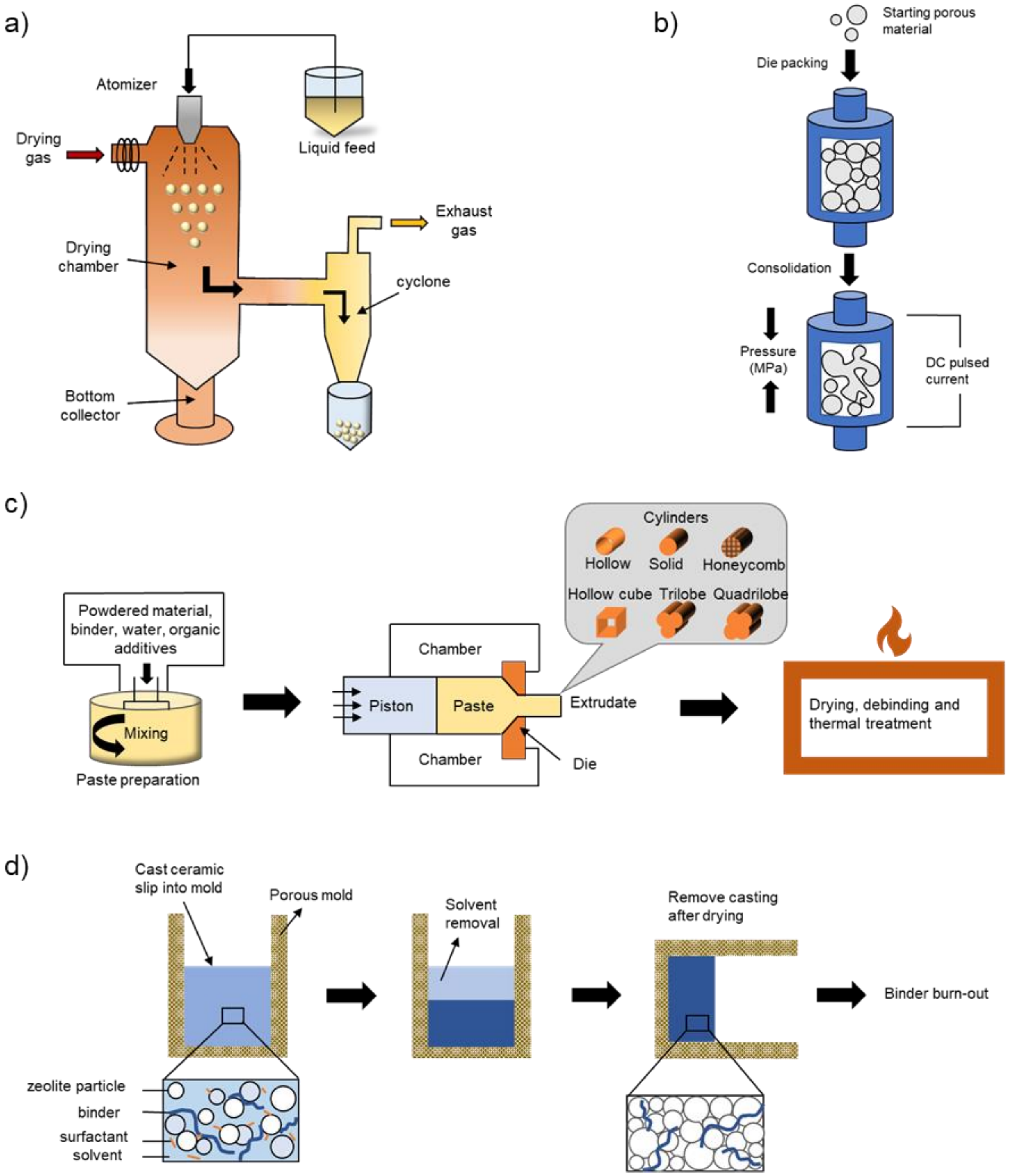

Figure 2. Schematic representation of conventional methods for shaping porous solids: (a) spray drying, (b) binder free pulsed current processing, (c) extrusion and (d) slip casting

Binder-free and robust monoliths can be directly produced using various types of porous powders by Pulsed Current Processing (PCP) as illustrated in Figure 2b. By using this process, porous particles can be partially fused with a minor loss of intrinsic surface area due to the high heating rates. The PCP production way requires identification of the temperature and pressure range at which mass transfer is insignificant and the characteristic porosity of starting powders is preserved. The binder-free PCP has been used to produce mechanically stable and hierarchically porous monoliths from microporous, mesoporous and macroporous powders.[36–38]

Extrusion is currently the most widely used manufacturing method to shape porous powders for adsorption and catalytic applications. A schematic diagram of the extrusion process is presented in Figure 2c where the process can be described as follow: (i) preparing a paste containing in particular the porous powder, (ii) extruding the paste through the die, (ii) drying and thermal treatment.[131] In order to be extruded, the paste must display appropriate rheological properties, such as a significant plasticity, along with sufficient cohesion to prevent surface and bulk defects in the extrudates. The extrusion process usually requires the addition of permanent binders (clay, SiO_2, $Al_2O_{3…}$) to reinforce the mechanical strength extrudate (green body) and monolith after thermal treatment. Various types of organic additives are also added to act as temporary binders, thickening agents and wetting agents, etc. Extrusion is able to produce commercial extrudates and honeycomb structures of adsorbents and catalysts such as zeolites A, X, ZSM-5, MOFs and porous carbon.

Slip casting (Figure 2d) offers the possibility to obtain complex shape from a suspension poured into a mold . Casting process involves dispersing the porous powders in a liquid or polymer with dispersant, plasticizer, binder and/or antifoaming agent, then mixing and deagglomerating them using ball milling or high shear mixer.[39] Slip casting is normally performed using Newtonian suspensions with an adapted solid loading for which the colloidal and rheological properties must be optimized. Nevertheless, materials containing organic compounds such as MOFs, COFs and carbonaceous can hardly be prepared by the methods mentioned above. On the one hand, their lower mechanical strengths limit the fabrication process with high pressure; on the other hand, the thermal treatment is not adaptable because the high temperature may destroy the porous structure because of decomposition of the organic part. Therefore, the monoliths of these materials are more often prepared *via* secondary growth on a ceramic grafted with organic linkers which can increase the adhesion between various components. Dip-coating, epitaxial formulating or reactive seeding are the most employed techniques to accomplish the monoliths fabrication with these materials. However, the processing time is long (several days to weeks) to produce a small loading and the secondary growth approaches generate wastes.[40–42] As a result, these approaches are not yet suitable for industrial applications. Moreover, traditional shaping processes have their drawbacks and limitations. For example, new molds must be manufactured in extrusion process to meet the needs of different applications, which will lead to an increase of labor, equipment and machining cost. Furthermore, conventional shaping methods are only able to provide simple structures or continuous channel designs. However, generating ultracomplex geometries is interesting from a transport perspective for the adsorption and catalysis processes, as it has been proven open channel designs can promote better contact with the fluids and enhance the transport properties.[43] The additive manufacturing technology can overcome the drawbacks of traditional shaping process to allow scaffold design to be more flexible and accurate.

3. AM Technologies

3D printing, also called additive manufacturing (AM) has been rapidly developed in the past decades. In recent years, many works related to 3D printing technologies in formulating porous materials have been conducted. The main steps of additive manufacturing process can be summarized as follow: (i) acquiring a 3D model using Computer Aided Design (CAD) or download models from an open-source provider; (ii) converting the 3D model to STL file format and using slicing software to slice the 3D model into 2D slayers; (iii) inputting instructions for the printer for each layer and building the part in the desired materials.[45]

Structures with highly complex geometries and interconnected holes (macropores) which are impossible to produce with traditional fabrication methods such as casting and extrusion, can be involved in 3D printing technique. It involves the design of the materials in 2D patterns corresponding to slices or sections through the final 3D geometry of the objects. The AM technologies can be classified as powder based or polymer based depending on the feedstock materials. In the powder based systems, a laser or electron beam is used to fuse partly the powder materials to interconnect them point by point, while polymer based systems use thermal energy or UV light to build the part point by point or layer by layer. In addition, polymer based (or slurry based) techniques, such as robocasting, fused deposition modelling, stereolithography and digital light processing, normally require a subsequent thermal treatment to remove the organic parts and to obtain the porous monoliths. It is worth noting that for a typical 3D printed ceramic structure, an additional sintering step is needed for densification, which maximizes mechanical properties. However, when maximum porosity and surface area are priority of the manufacturing process, sintering is not an option due to the densification would cause the collapse of structures of most porous solids at temperature above 800 °C. Among many different AM technologies, only those relevant to porous solids are considered and introduced in this review.

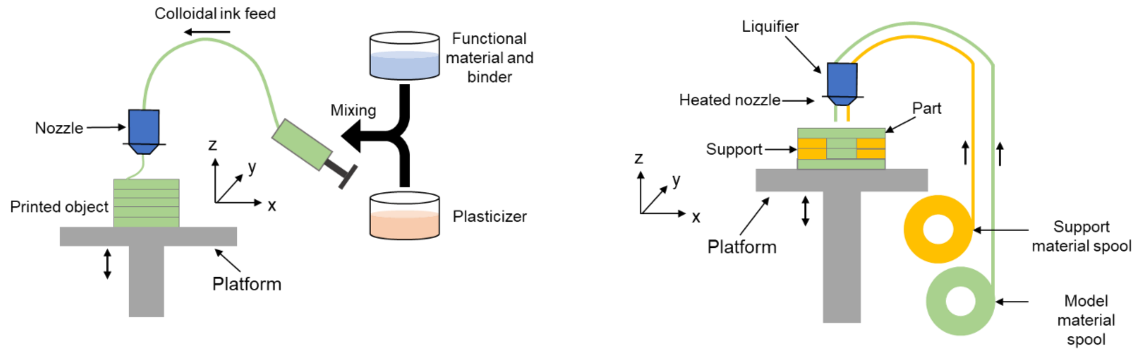
(a) Robocasting

(b) Fused Deposition Modelling (FDM)

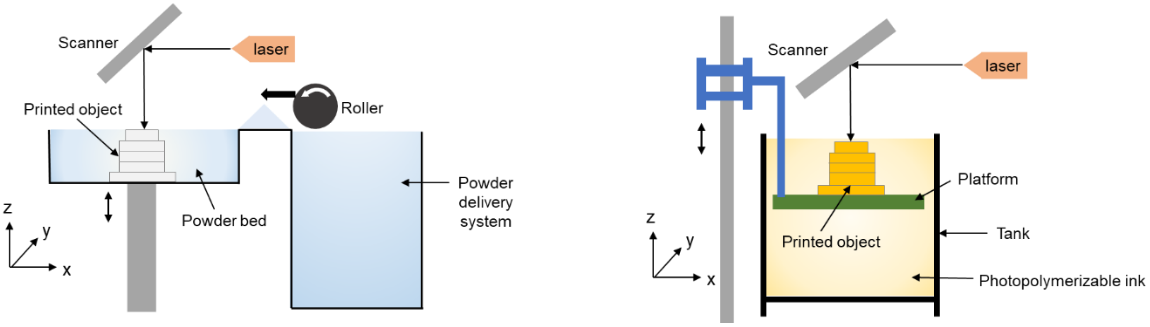
(c) Selective Laser Sintering (SLS)

(d) Stereolithography (SLA)

Figure 3. Different 3D printing techniques. (a) robocasting (b) fused deposition modelling (c) selective laser sintering and (d) stereolithography.

3.1. Robocasting

Robocasting, also termed as Robotic Deposition, Direct Ink Write (DIW) or 3D Fiber Deposition (3DFD), is an additive manufacturing technique in which filaments of paste-like materials are extruded from a small nozzle while the nozzle is moved across the platform.[44] The inks usually contain functional materials, binders, additives such as dispersant or plasticizer to adjust the rheology properties. The advantages of robocasting are that the printing process is conducted at room temperature and the ink material is self-supporting during assembly. After printing, the structure can either be thermally cured at high temperature or cured by UV light (in this case, a photoinitiator has been introduced in the ink formulation). A typical setup for robocasting is shown in Figure 3a.

This technique is predominantly intended for printing ceramics,[45] but it can be used to print almost any powder based materials including zeolites,[46] MOFs,[47] and carbonaceous material[48] as long as the fluid properties are adjusted. In general, the formulated printing ink has to match the following requirements: (i) reversible shear-thinning behavior, and viscosity should be low enough (in the range of 10–100 Pa s) at high shear rate to facilitate the extrusion and be high enough at static state to retain the shape afterward, (ii) free of particle agglomerates to avoid clogging the nozzle, and (iii) possessing relatively high yield stress ($\tau_y > 200$ Pa) to allow self-support and fabrication of high aspect ratio structures. The layers printed by robocasting method are relatively thick (usually 200-800 μm) as the printing resolution is very limited by the nozzle size. [44]

3.2. Fused Deposition Modelling

Fused deposition modelling (FDM), also known as fused filament fabrication (FFF) is a processing where a thermoset polymer is heated above its glass-transition temperature (T_g) and extruded through a nozzle. The polymer in semi-molten state solidifies upon cooling after deposition on the printer bed by forming bonds between layers *via* chain diffusion, resulting in mechanically stable prints. The print head can be moved under computer control in the x and y directions to deposit one horizontal plane, while the printer bed is moved vertically (in the z direction) to create the printing patterns layer by layer (Fig. 3b). A wide range of process parameters can influence the final mechanical properties: layer thickness, nozzle diameter, deposition speed, contour width, top/bottom thickness, building orientation, extrusion temperature and bed temperature.[49]

The most commonly used thermoset polymer in FDM is acrylonitrile butadiene styrene (ABS), followed by polycarbonate (PC), polylactic acid (PLA), polyphenylsulfone (PPSF), nylon and Torlon.[50] By combining a functional material such as graphene,[51] carbon fibers,[52] ZrO_2[53] and iron,[54] the composite filament will induce changes in printing properties such as the temperature of the nozzle and of the bed, and flow rate. As a result, some trial and error may be required to optimize the printing process. There are several challenges associated with FDM, including under or over extrusion, temperature variation and strong dependence on environment conditions. Therefore, the failure rate is relatively higher (20% among unskilled users) for FDM compared to other printing techniques.[55]

3.3. Selective laser sintering (SLS)

Selective laser sintering (SLS) is a class of Laser Powder Bed Fusion (LPBF). The process involves fusing powder particles from a powder bed using laser heat, then cooling to solidify to form a 3D object.[56] Unlike selective laser melting (SLM), the temperature employed in this process is lower than the melting point of the printing material. As illustrated in Figure 3b, the laser is traced over a cross section of the printing object in the xy plane. Once a layer is sintered, the platform will be lowered by one-layer thickness, and a new layer of material is applied on the top by a roller on the printer. After the process is completed, the printed object can be obtained through sieving the unfused material. The particle size in the printing material must be closely controlled since it can have an impact on the physical/chemical stability and content uniformity of the printed object.[56]

This technique is compatible with metals, ceramics, and a few thermoplastic polymers like polycarbonate (PC), thermoplastic elastomers (TPEs), polyetherketone (PEK), polyamide 11 (PA11) and polyamide 12 (PA12) due to the unavailability of other materials in powdery form.[57] PA12 remains the most commonly used polymer for laser sintering in the production of functional plastic parts with improved mechanical properties, either as a single material or in a blended material system. In recent years, researchers have reported the fabrication of monolithic structures of MOFs and zeolites using SLS. This involves mixing powders of the MOF/zeolite with selected polymers.[57–59] It is interesting to note that SLS printing can create internal porosity within the structure, allowing for the pores of filler material to remain accessible. However, the addition of fillers to polymeric materials can lead to changes in the melting and crystallization temperatures. Therefore, prior to the SLS processing, the processing temperatures must be estimated according to differential scanning calorimetry (DSC).[57]

3.4. 3D printing *via* photopolymerization

3.4.1. Photoinitiators/ Photoinitiating systems (PIs/PISs) and monomers

The PI is mainly responsible for converting photolytic energy into active substances during photopolymerization based AM, and the generated active substances initiate deep-curing of monomers/oligomers. Since the PIs impose the speed of photocuring process and also affects the physical and mechanical properties of the printed object, it plays a key role in the entire photopolymerization based AM process. Photoinitiators are typically classified into two groups: Type-I and Type-II. Type-I PIs absorb radiation and undergo bond cleavage from an excited state, generating initiating radicals. On the other hand, Type-II PIs undergo hydrogen abstraction from a co-initiator (hydrogen donor), resulting in the formation of two free radical species (Figure 4). The homolytic cleavage of Type-I PIs can occur at the α-position (major) or β-position (minor) of the carbonyl group, depending on the bond strengths. Type-II PIs, on the other hand, require a co-initiator such as tertiary amine, ether, ester, thiol, etc., to pass hydrogen to the triplet state PI, producing a less reactive ketyl radical and a highly reactive donor radical.[136]

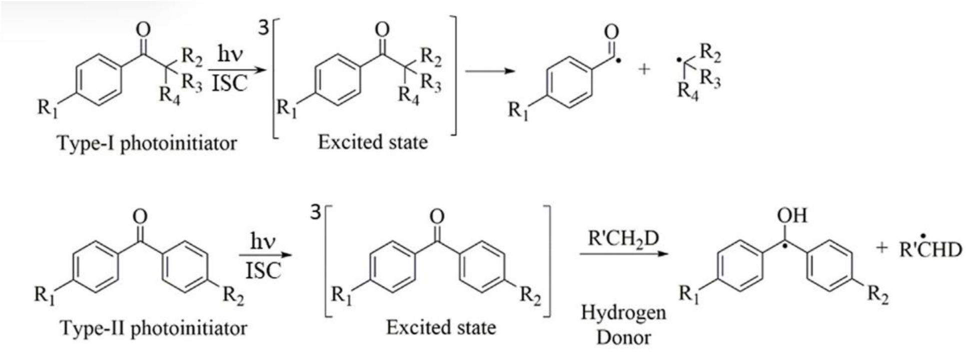

Figure 4. Reaction mechanisms with Type-I and Type-II photoinitiators. (Reproduced from ref. 136 with permission. Copyright 2019, Elsevier.)

Typically, epoxides, (meth)acrylates are the most employed monomers or oligomers in 3D printing by photopolymerization (Figure 5).[70] Acrylate or methacrylate monomers undergo polymerization via a radical curing mechanism, resulting in a rapid curing speed. Once the light source is removed, the curing process stops without further progression, demonstrating excellent controllability. Furthermore, the properties of (meth)acrylates are variable and easily modified thanks to their widely available structures.[71] It was reported the combination of acrylate and methacrylate is preferable due to the slow curing nature of methacrylates and to the distorsions observed in the printed object with pure acrylate system.[71] The drawback of the (meth)acrylates is that they undergo shrinkage during polymerization, which depends on the molecular structure. Cycloaliphatic and aromatic acrylates shrink less than common diluents (ie. bis-GMA shrinks about 5%, while HDDA shrinks about 18-22 vol%).[72,73] On the other hand, epoxides cure through the cationic curing mechanism, which exhibits considerably slower curing kinetics compared to acrylates. However, epoxides also demonstrate reduced shrinkage during the curing process. The dark curing property (resin continues to cure even after the light has been turned off) and high viscosities present challenges in controlling the polymerization process of epoxides.[74] Thiol-ene and thiol-yne (Figure 5) are also well-represented in DLP due to their ability to reduce the shrinkage and oxygen inhibition associated with acrylates.[75]

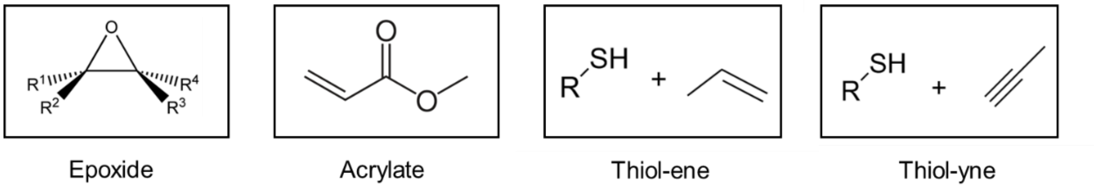

Figure 5. Common functional groups employed in 3D printing by photopolymerization. R = alkyl group

3.4.2. Stereolithography (SLA)

The SLA technique has become one of the most prominent and popular printing technology since its invention in 1980s by Hull.[60] In this process, a light source of a particular wavelength (usually in ultraviolet range) is used to selectively cure a liquid surface of a photopolymerizable monomer, containing small amounts of photoinitiators and additives. The light-activated process converts the liquid monomer into solid resin, with the light scanning on the liquid surface point-to-line, line-to-layer, then layer-by-layer. As illustrated in Figure 3d, the light source can move along the x, y directions to create a horizontal pattern while the platform is programmed to move along the y axis. In some cases, a wipe blade is needed to level off the liquid surface before printing the next layer. The main advantage of SLA is the high resolution (up to 10 µm) and possibility to fabricate high surface quality.[61]

The SLA of porous solids proceed with the dispersion of porous powder, down to micro/nano-size, into the photocurable medium, together with inorganic and organic additives. Typically, polymerization only takes effect in the monomer phase under light irradiation. Once the porous powders are uniformly surrounded by cross-linked polymer network, the pre-designed shape of each layer is formed by photopolymerization until the entire 3D part is built up. Then, moisture is removed and organic parts are decomposed by thermal treatment and a porous monolith is achieved.

To successfully carry out the printing process on the filled resin, several requirements must be fulfilled. First, it is necessary for the printing slurry to possess appropriate rheological properties, such as long-term stability and suitable viscosity. The porous solids must be homogeneously dispersed in the photopolymerizable medium and remain stable without settling or agglomeration before use. The suspension should maintain a sufficient fluid property for proper flow during printing process, whether comparable to commercial resin (< 3000 mPa.s) in the past or tens of Pa.s at a shear rate of 1000 s^{-1} for modern technologies.[62,63] Nevertheless, a higher solid loading is favorable for less shrinkage and greater density (better mechanical strength) after thermal treatment, while higher solid content results in unfavorable viscosity and possible segregation. Therefore, compromise must be found to prepare suitable printing slurry containing porous solids. Another challenge is the light scattering arising from the solid particles. As a consequence, poor light penetration and undesirable broadening of the curing area may occur, resulting in poor resolution. In addition, the curing depth which is associated with the layer thickness, is strongly affected by the solid particle size, light source power, filler volume fraction and the difference between the reflective indexes of the filler and the resin.[64] The optical losses due to reflection, scattering, or absorption of the filler particles can be highly challenging to the process.

3.4.3. Digital light processing (DLP)

With similar set up as SLA, DLP technology uses a projector as the light source. The projector light is cast by a patterned mask and transferred to the photopolymerizable slurry to create an integral image at once. Finally, layer by layer, the 3D structure is printed. In early stages of development, physical masks were used by Nakamoto and Yamaguchi in 1996.[65] Later on, Bertsch et al. developed a liquid crystal display (LCD) as the dynamic mask generator to improve the printing process.[66] The LCDs were further replaced by digital micromirror devices (DMDs) from Texas Instruments thanks to its high resolution and contrast in the light display.[67–69] The DLP have advantages over the conventional SLA point-line-layer process due to its ultra-fast light switching and integral projection, allowing the printing time to be significantly reduced. Furthermore, very good feature resolution (up to several µm) makes DLP a promising technique to fabricate parts with high accuracy and high speed.

Similar to SLA technology, the light source can either be positioned below or above the tank, referred to as "bottom-up" or "top-down" approach respectively (Figure 6). In the bottom-up setup (the platform moves up for every layer), the parts are fabricated from the bottom surface of the tank and the subsequent layers are cured underneath the previous layers. In the top-down version, parts are fabricated from a support beneath the resin liquid level and the platform moves down for every layer, resulting in new layers cured above the previous one. Santoliquido et al. studied the difference between the two approaches in fabricating ceramic monolith.[76] The advantages and inconveniences are summarized in Table 2. The "top-down" approach presents some limitations for 3D printing bulk components with large surface areas and cross sections, but it makes possible to obtain rather smooth surfaces. "Bottom-up" method is most used in the actual manufacturing process. Its main restriction is related to the small length/width ratio associated to the printed object, but more defined details and greater precision can be obtained.

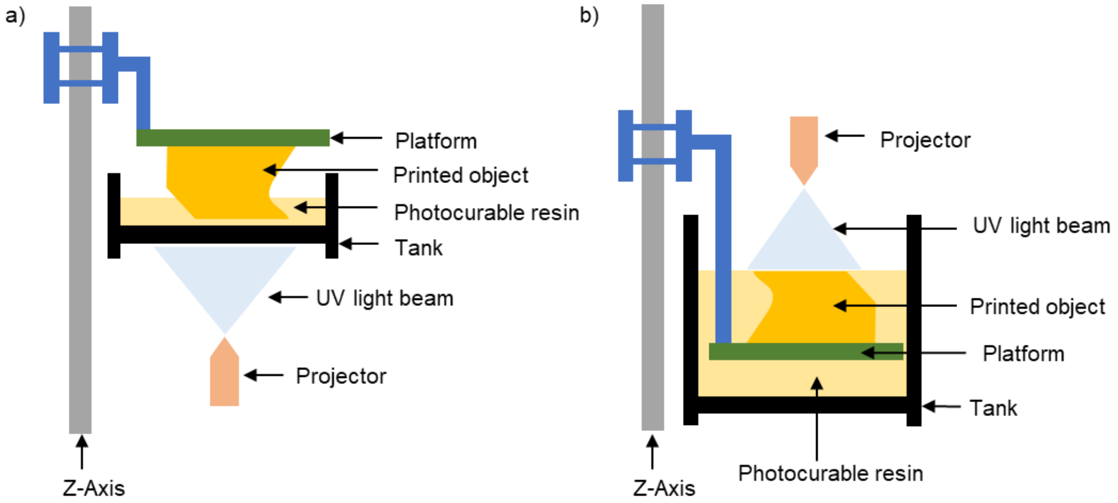

Figure 6. Digital Light Processing (DLP) and Stereolithography (SLA) technologies with: (a) "bottom-up" set up; (b) "top-down" set up.

Table 2. Main differences between DLP printing approaches (reproduced from ref. 76 with permission. Copyright 2019, Elsevier.)

"Bottom-up" approach	**"Top down" approach**

A small amount of photosensitive slurry is required	More photosensitive slurry is needed in order to cover completely the printed part
Less exposure time needed because the photopolymerization is conducted without the presence of oxygen	Higher exposure time is required due to the slurry in contact with oxygen, resulting in inhabitation of the polymer chain growth by capturing free radicals.
Layer thickness is constant, precise and easily controllable	Layer thickness is not constant, homogenous and easily controllable. The problem intensifies with increasing the viscosity of slurry and cross-sectional solid area of each slice
Obtaining detailed and accurate object is easier	Obtaining accurate and detailed components is more difficult and laborious
More suitable for processing bulk components (macroporosity <78%)	More suitable for processing porous components (macroporosity >78%)
Difficulty in printing components which are too slender (length/width ratio >3) due to the gravity force	No limitations about the shape and dimensions of the printed object since the object stands on the platform
Presence of a detachment movement at every slice, causing unwanted stresses and deformation, leading to possible failures during printing or deformations during thermal treatment	No detachment movement at every layer is required (semi-continuous operation possible)
The light irradiation must pass through the transparent tank bottom with a consequent reduction of the light intensity	The light directly reaches the photosensitive slurry, without any reduction in intensity
More complicated printer parts may wear out and require periodic replacement, resulting in less reproducible results	Fewer components that wear out and must be replaced regularly. Results obtained are more reproducible
Longer printing time due to the detachment movement performed at each layer	Shorter printing time despite the exposure time is longer

4. Printing strategies of structured porous materials

In this part the printing methods are classified into three categories: (i) *via* extrusion, (ii) *via* photopolymerization, (iii) from powder-based technologies. We mainly focus on the works and advances within the past 5 years. The scaffold preparation, the relevant applications, the advantages and the limitations of each method will be discussed.

4.1. 3D printing *via* slurry extrusion

Robocasting (or DIW) involves preparation of a formulation composed of a commercial or synthesized porous material (zeolite, MOF, COF, active carbon, etc.) a solvent, a binder, a plasticizer and additives to achieve a proper rheological property for extrusion. The formulation is usually rolled for some time before printing to ensure the homogeneity and proper binding between different components.[47,77,78] A thermal treatment is required in most of the case to make the porosity of the porous material accessible: it allows the decomposition of organic compounds as polymeric plasticizer for example. When it comes to MOFs and COFs, the conventional step of the thermal treatment cannot be applied as they may decompose under high temperature. It is therefore necessary to choose specific solvents and plasticizers for these materials. Nevertheless, printing *via* extrusion is still the most popular way to shape porous materials as it enables a cheaper and faster manufacturing.

4.1.1. 3D printing *via* extrusion for adsorption

A list of 3D-printed monoliths prepared *via* extrusion for adsorption applications is reported in Table 3. Zeolite materials can be shaped into desired structures with this method using high solid content slurries (up to 90 wt%). In a representative study, Thakkar and coworkers reported the fabrication of honeycomb zeolite monoliths (5A and 13X) *via* DIW using bentonite as the permanent binder, and Polyvinyl alcohol (PVA) and carboxymethyl cellulose (CMC) as the temporary binders (Figure 7a).[78] By a thermal treatment at 700 °C, the organic parts (namely PVA and CMC) were then removed resulting in increasing the mesoporosity. Pure inorganic monoliths were thus obtained with zeolite content up to 92.8 wt% (Figure 7b-e). These monoliths present great compressive strength with 0.69 MPa for 13X and 0.35 MPa for 5A (Figure 7g), which is higher than for the zeolite pellets used in NASA's CO_2 removal system.[79] Finally, these monoliths exhibited significant CO_2 adsorption rate: the adsorption capacity of monoliths 13X and 5A represents 87% and 89% respectively of that of the corresponding zeolite powder (Figure 7f). The decreasing in CO_2 adsorption capacity is mainly due to the presence of bentonite binder. The use of binders in extrusion process will be discussed in section 4.1.2.

Table 3. List of monoliths with their fabrication conditions through slurry extrusion for adsorption applications

Active material and content	Binder	Solvent	Plasticizer	Post treatments	Applications and capacity	ref
zeolite 13X (29 wt%) + activated carbon (12 wt%)	CMC	DI water	-	room temp, 48 h	electrical swing adsorption (ESA) for CO_2: 0 °C 0.15 bar (3.5 mmol/g)	48
zeolite 13X (up to 90 wt%)	bentonite and PVA	DI water	CMC	drying at 100 °C then calcination at 700 °C	adsorption of CO_2: 25 °C 1 bar (4.3 mmol/g)	78
zeolite 5A (up to 90 wt%)	bentonite and PVA	DI water	CMC	drying at 100 °C then calcination at 700 °C	adsorption of CO_2: 25 °C 1 bar (4.5 mmol/g)	78
zeolite 13X/5A (13 wt%)	Torlon	DI water and NMP	PVP	solvent exchange to remove NMP then drying at 60 °C under vacuum for 2 h	removal of CO_2 from flue gas: 35 °C 1 bar (1.83 mmol/g for 13X and 1.51 mmol/g for 5A)	86
SAPO-34 (50 wt%) + graphite (5 wt%)	CMC	DI water	PAA	room temp, 48 h	separation of CO_2/N_2: 30 °C 1 bar (3.4 mmol/g)	46
zeolite 13X (84 wt%)	HNTs and silica	DI water	HPMC	calcination at 650 °C, then hydrothermal crystallization to transform HNTs into zeolite	CO_2 adsorption: 25 °C 0.02 bar (2.5 mmol/g)	87
zeolite ZSM-5 (65 wt%)	bentonite, colloidal silica	DI water	-	drying at 20 °C then calcination at 550 °C for 3 h	29 °C 30 bar: (2.2 mmol/g for CO_2, 1.3 mmol/g for CH_4, 0.9 mmol/g for N_2)	88
aminosilica (90 wt%)	bentonite	DI water	CMC	drying at 80 °C for 2-3 h then calcination at 550 °C	CO_2 capture: 25 °C 1 bar (up to 2.23 mmol/g)	89
MOF-74 (13.0 wt%)	Torlon	NMP, DMF, DI water	PVP	solvent exchange	CO_2 adsorption: 25 °C 1 bar (0.6 mmol/g)	82
MOF HKUST-1(17.3 wt%)	Torlon	NMP, DMF, DI water	PVP	solvent exchange	CO_2 adsorption: 25 °C 1 bar (1.2 mmol/g)	82
ZIF-8 (66.7 wt%)	bentonite	DI water	CMC	thermal treatment at 450 °C under Ar	biobutanol recovery: 40 °C (0.24 g/g butanol absorbed)	84
Cu-BTC (up to 13 wt%)	Sodium alginate, gelatin	DI water	-	ion exchange with $CaCl_2$ (4 wt%) then freeze-drying at 80 °C	organic dyes (MB) removal: 25 °C, 20 ppm solution (99.8% removal)	80
MOF-74(Ni) (80 wt%)	bentonite	DI water, EtOH	PVA	drying at 100 °C	CO_2 adsorption: 25 °C 1 bar (4.0 mmol/g)	47

UTSA-16(Co) (85 wt%)	bentonite	DI water, EtOH	PVA	drying at 100 °C	CO_2 adsorption: 25 °C 1 bar (3.0 mmol/g)	47
HKUST-1 (16 wt%)	HEC	DI water	PVA	drying at 90 °C under vacuum	methane adsorption: 25 °C 35 bar (81 g/kg)	83
ZIF-8 (20 wt%)	HEC	DI water	PVA	drying at 90 °C under vacuum	methane adsorption: 25 °C 30 bar (59 g/kg)	83
UiO-66-NH_2 (17 wt%)	HEC	DI water	PVA	drying at 90 °C under vacuum	methane adsorption: 25 °C 20 bar (30 g/kg)	83
ZIF-8 (40 wt%)	PLA	$CHCl_3$, ethyl acetate	-	Solvent exchange with methanol and drying at 75 °C	N_2 adsorption: -196 °C (S_{BET}=531 m^2/g)	81
ZIF-8 (40 wt%)	TPU	DMF, acetone	PVDF-HFP	drying at 75 °C	N_2 adsorption: -196 °C (S_{BET}=706 m^2/g)	81
COF SNW-1 (9.45 wt% in paste)	-	DI water	-	~4 °C for 3 days then drying at 80 °C under vacuum	CO_2 adsorption: 25°C 1 bar (1.85 mmol/g)	85

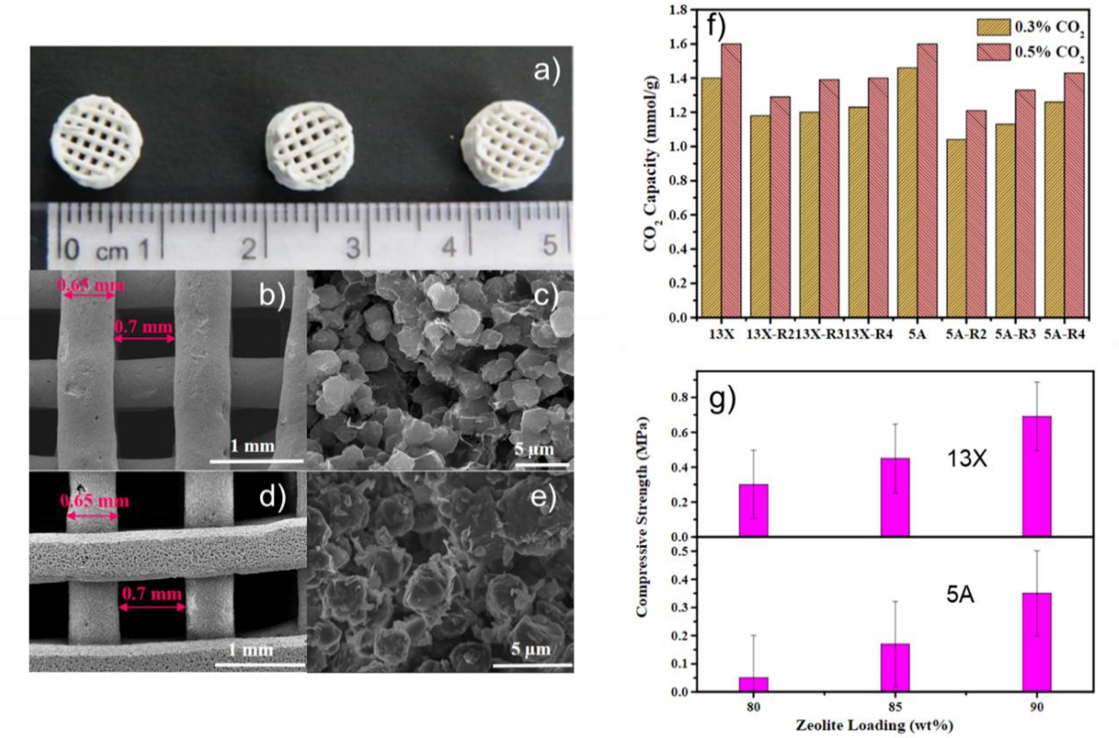

Figure 7. (a) 3D-printed self-standing zeolite 13X monoliths by DIW, SEM images of monoliths (zeolite content: 90 wt%) after thermal treatment (b-c) 13X monolith and (d-e) 5A monolith, (f) CO_2 adsorption capacities for 3D-printed monoliths and zeolite powders obtained at 25 °C using 0.3% and 0.5% CO_2 in N_2 (R2-R4 for zeolite content equals to 80, 85, 90 wt% respectively), (g) compressive strength versus zeolite loading (wt%). (Reproduced from ref. 78 with permission. Copyright 2016, American Chemical Society.)

In another work, Pei and coworkers developed a printable ink for DIW by adding Cu-BTC to a mixture of sodium alginate and gelatin.[80] In order to investigate the influence of different geometries on adsorption capacity, three different patterns (square, hexagon, and circle) were manufactured. An instantaneous cross-linking with through Ca^{2+} provides sufficient mechanical stability after printing (Figure 8a). The 3D-printed adsorbents were used to adsorb methylene blue (MB) in aqueous medium. The authors have also investigated the influence of MOF content and extrusion pressure on rheological properties (Figure 8b). The results suggested that the MOF content should not exceed 13 wt% in the printing slurry to avoid nozzle clogging problem. Furthermore, the printed MOF/CA-GE sample (active material: MOF, loading = 13 wt%) exhibited high MB adsorption efficiency up to 99.8% (equivalent to 15.4 mg per gram of active material whose BET surface area is 1562 m^2/g). Additionally, the regenerated adsorbents (by soaking in HCl solution) retains a MB removal efficiency above 92% after at least 7 adsorption/regeneration cycles. In contrast, the Cu-BTC as powder was quite unstable and its adsorption capacity has decreased significantly after one cycle. For the printed geometries, hexagon structure displayed the highest porosity (59.2%) and the best saturation adsorption rate (Figure 8c). As such, this study demonstrated the benefit of applying a 3D technology with hydrolytically stable MOF. Some other types of MOFs have also been used in DIW or FDM technique[81] for CO_2,[47,82] methane,[83] and butanol adsorption[84].

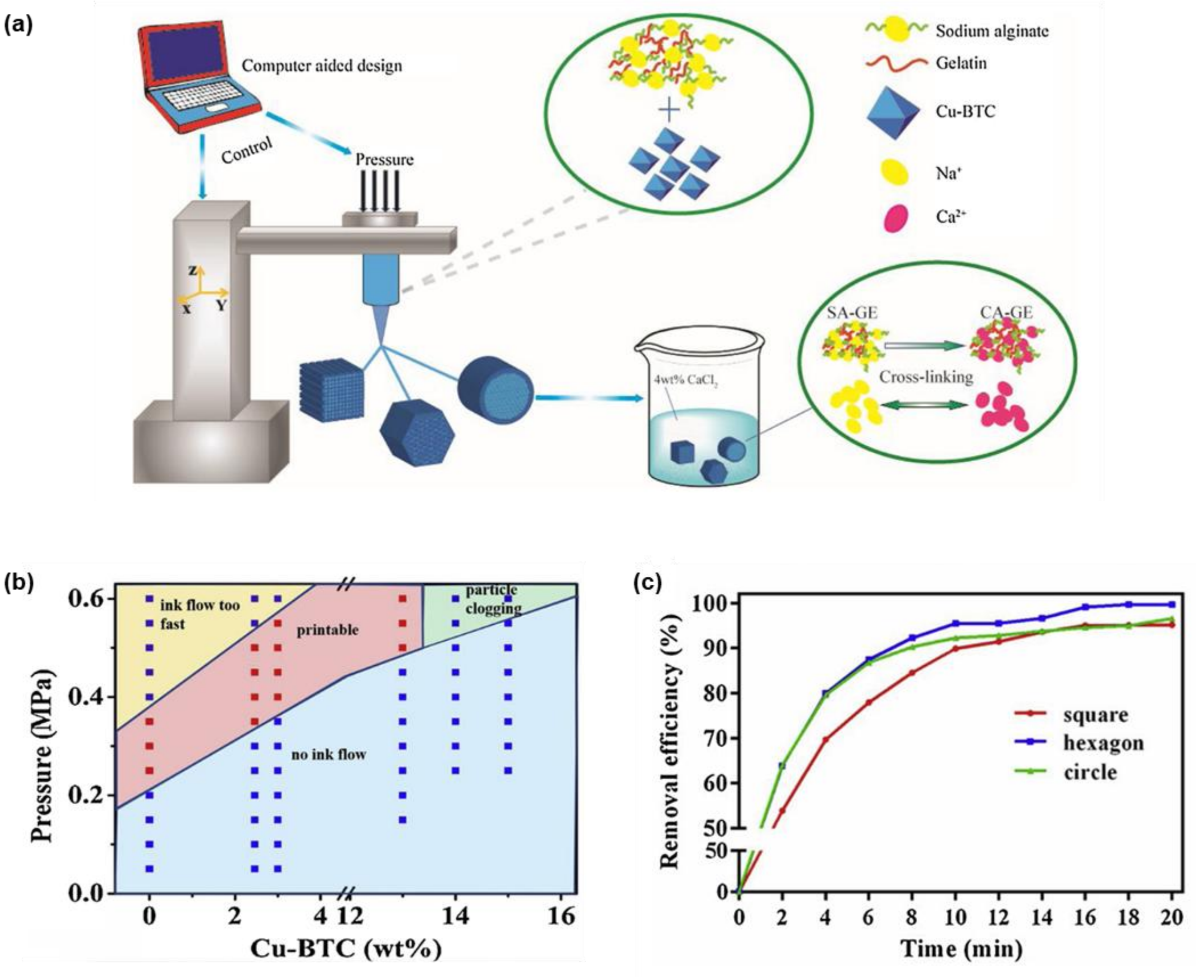

Figure 8. (a) The preparation of 3D-printed adsorbents with three different geometries (square, hexagon, and circle) and the cross-linking with $CaCl_2$ solution to enhance the mechanical properties (SA-GE=sodium alginate, CA-GE=calcium alginate), (b) printability of Cu-BTC/SA-GE mixed inks, (c) MB adsorption performance of adsorbents with printed patterns with three different geometries (MOF loading=13 wt%) over different time. (Reproduced from ref. 80 with permission. Copyright 2019, Elsevier.)

Recently, Liu et al.[85] elaborated binder-free COF monoliths for CO_2 adsorption by preparing a printable paste containing COF (SNW-1) and deionized water (DI water). They also added an organic binder (F-127) to study its influence on CO_2 adsorption. For optimal printability, the solid content was finally fixed at 9.45 wt% and the printed monoliths were then dried on different substrates. It was found that porous, hydrophilic and low surface energy substrates lead to more uniform shrinkage and more water evaporation, which allows to avoid cracks and retain the shape of monoliths (Figure 9a). On the other hand, the adsorption results showed the binder-free SNW-1 monolith exhibited similar BET surface (794 vs 830 m^2/g) and comparable CO_2 adsorption capacity to the COF powder. However, the addition of binder drastically reduced the adsorption capacity (Figure 9b). This study opened a new gate in the domain of 3D-printed COF monoliths.

Compared to other AM techniques, DIW is faster and cheaper in terms of the cost, open source printer units and versatility.

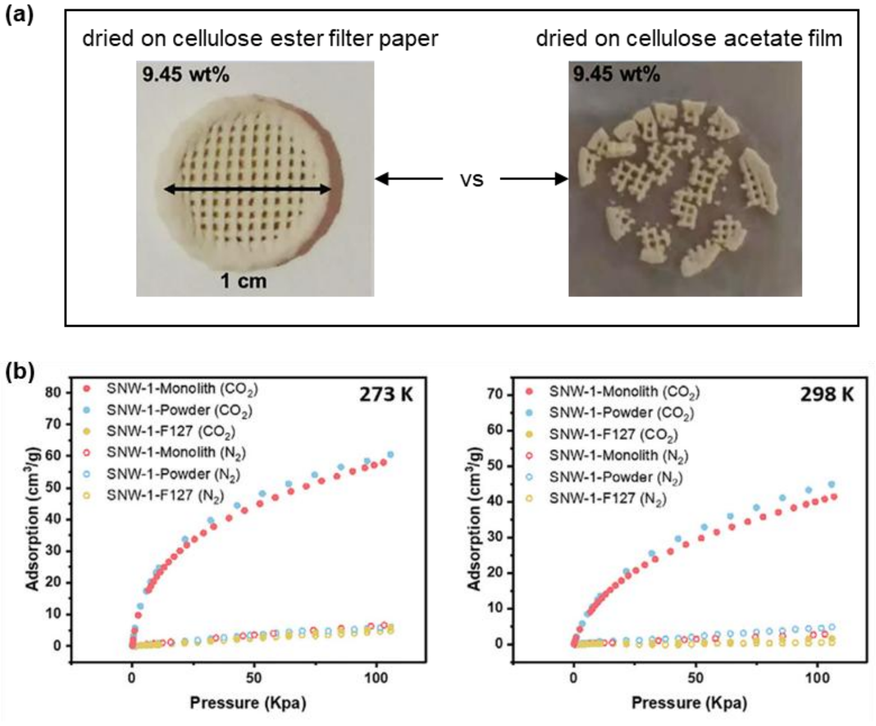

Figure 9. (a) appearance of the 3D-printed SNW-1 monolith (9.45 wt%) dried on cellulose ester filter paper (left) and cellulose acetate film (right); (b) CO_2 and N_2 adsorption curve of SNW-1 monolith, SNW-1 powder, and SNW-1/F127 monolith at 273 K (left) and 298 K (right). (Reproduced from ref. 85 with permission. Copyright 2020, Elsevier.)

4.1.2. 3D printing *via* extrusion for catalytic applications

Table 4 summarizes recent studies concerning 3D-printed MOFs, zeolite, and alumina for catalytic applications. Similar to 3D-printed adsorbents mentioned in section 4.1.1, the pre-synthesized porous materials have been investigated to prepare monoliths with more complicated geometries to solve issues such as pressure drop in industry for catalytic reactions. For instance, Li and coworkers prepared 3D printed HZSM-5 (MFI type) and HY (FAU type) monoliths by direct ink write for catalytic cracking of n-hexane.[90] The printing slurries were prepared with 87.5 wt% of zeolite, 10 wt% of bentonite, 2.5 wt% of methyl cellulose (MC) and DI water was added to adjust the viscosity. The printed monoliths helped to maintain the conversion of hexane at a high level with time (Figure 10a, b). To further modify and improve the performance of printed catalysts, SAPO-34 was grown on the zeolite monolith surface *via* secondary growth method. As illustrated in Figure 10b and 10d, the HY monolith coated with SAPO-34 (named SYM in the figure) exhibited higher conversion and BTX selectivity (butanol-toluene-xylene) compared to the powder (named YP) and monolith without coating (YM). As for HY, the highest selectivity to light olefins (53.0%) was found over ZSM-5 monolith without coating (ZM) at 650 °C in 24 h (Figure 10c).

Active material and content	Binder	Solvent	Plasticizer	Post treatments	Applications and capacity	Ref
MFI zeolite (ZSM-5) (87.5 wt%)	bentonite	DI water	CMC	drying at 100 °C then calcination at 550 °C for 5 h	methanol to dimethyl either (DME) (MeOH conversion ~95% and DME selectivity ~25% at 320 °C)	77
Monolith of ZSM-5 (87.5 wt%) coated with SAPO-34	bentonite	DI water	CMC	drying at 100 °C then calcination at 550 °C for 5 h	methanol to dimethyl either (MeOH conversion ~74% and DME selectivity ~15% at 320 °C)	77
ZSM-5 (65 w%)	bentonite/colloidal silica/$AlPO_4$	DI water	CMC	calcination at 550 °C for 3 h	methanol to olefin (MTO)	91
ZSM-5 (87.5 wt%) with metal dopants (Ga, Cr, Cu, Zn, Mo, Y)	bentonite	DI water	CMC	calcination at 600 °C for 6 h	methanol to hydrocarbon (MTH) (Y- and Zn- doped ZSM-5 monolith exhibited higher yield of olefins)	94
ZSM-5 (85 wt%) with metal dopants (V, Zr, Cr, Ga)	bentonite	DI water	CMC	calcination at 550 °C for 6 h	cracking of n-hexane (highest hexane conversion with Cr dopant: 85%)	95
ZSM-5 (87.5 wt%)	bentonite	DI water	CMC	calcination at 550 °C	cracking of n-hexane (higher olefin selectivity compared to powder; higher BTX selectivity when coated with SAPO-34)	90
FAU zeolite (HY) (87.5 wt%)	bentonite	DI water	CMC	calcination at 550 °C	cracking of n-hexane (higher olefin selectivity compared to powder; higher BTX selectivity when coated with SAPO-34)	90
α-Al_2O_3 (30 vol%)	PEI	DI water	HPMC	sintering at 1500 °C in air for 2.5 h	Hantzsch and Biginelli reactions	97
KMoCo/ZSM-5 (K, Mo, Co were in situ grown onto channels of zeolite)	bentonite, colloidal silica	DI water	starch	drying at 25 °C for 24 h then calcination at 550 °C	higher alcohols synthesis (selectivity as 56% towards higher alcohols)	96
Porous carbon	SiO_2	DI water	starch/gelatin	freeze-drying, carbonization at 1100 °C for 2 h	oxidation of benzyl alcohol (conversion was enhanced by SiO_2 and selectivity was maintained)	98
Fe doped SiC	PEI	DI water	-	sintering at 1200 °C	wet peroxide oxidation processes	99

Table 4. List of monoliths fabricated through slurry extrusion for catalytic applications

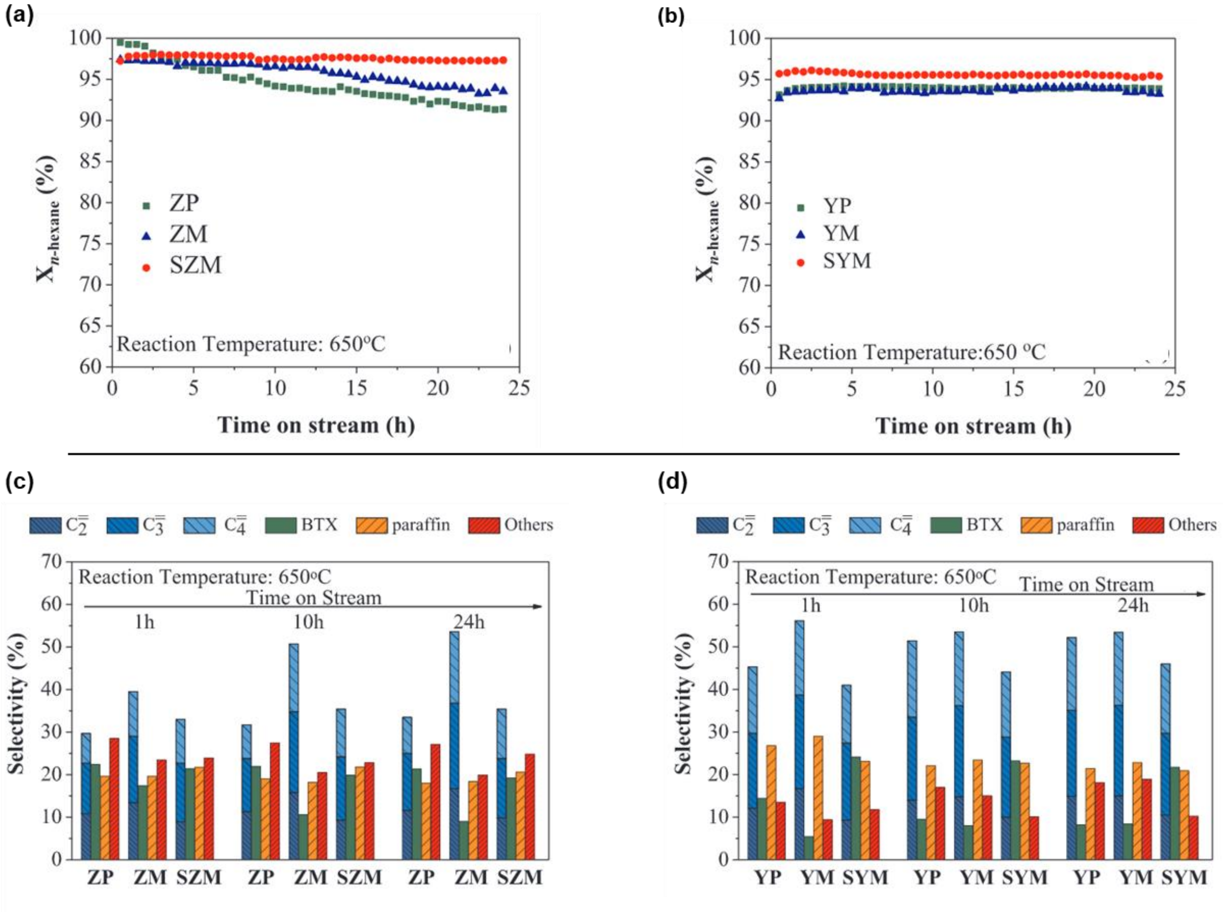

Figure 10. Conversion of n-hexane as the function of time on stream at 650 °C on (a) HZSM-5 and (b) HY; product distribution on (c) HZSM-5 and (d) HY. (P=powder, M=monolith, S=SAPO-34, Z=ZSM-5, Y=HY). (Reproduced from ref. 90 with permission. Copyright 2017, Elsevier.)

In another work, Lefevere and coworkers discussed the binder system for printing ZSM-5 hierarchical monolith *via* DIW.[91] Three permanent binders namely bentonite, colloidal silica and aluminophosphate were tested for a mono or binary binder system. The printing slurry was composed of ZSM-5 powder (65 wt%), binder (35 wt%), water and a small amount of methylcellulose. The results demonstrated that binders have an impact on the flow properties, drying methods, porosity and acidity of the final product. More precisely, bentonite can act as plasticizer and achieve the desired shear thinning effect while silica and aluminophosphate needed additional methylcellulose to adjust the rheological properties (Figure 11a). However, bentonite induced severe shrinkage (11.1%) upon drying, resulting in ruptures in the structures. Therefore, drying under controlled atmosphere must be applied to monoliths containing bentonite while monoliths with silica needed rapid drying to avoid collapse (Figure 11b-e). Moreover, Table 5 summarizes the number of acid sites and the crush strength of pure zeolite and structures with mono/binary binder system. A decrease in number of acid sites (per surface and per weight) can be observed for the structures with bentonite or silica binder. This decrease can be related to the exchange of cations from the binder with the acid sites of ZSM-5. Some synergic effects were observed in the binary binder system, indicating a clear interaction between different binders. The combination of bentonite/AlO$_4$ has less influence on zeolite’s acidity compared to when bentonite is used alone. This effect is likely due to the interaction between bentonite and the excess of phosphate present in the aluminophosphate solution. In terms of mechanical properties, bentonite/AlPO$_4$ binary binder system showed the highest crush strength (1.54 MPa), which was much higher than when the binders were used alone.

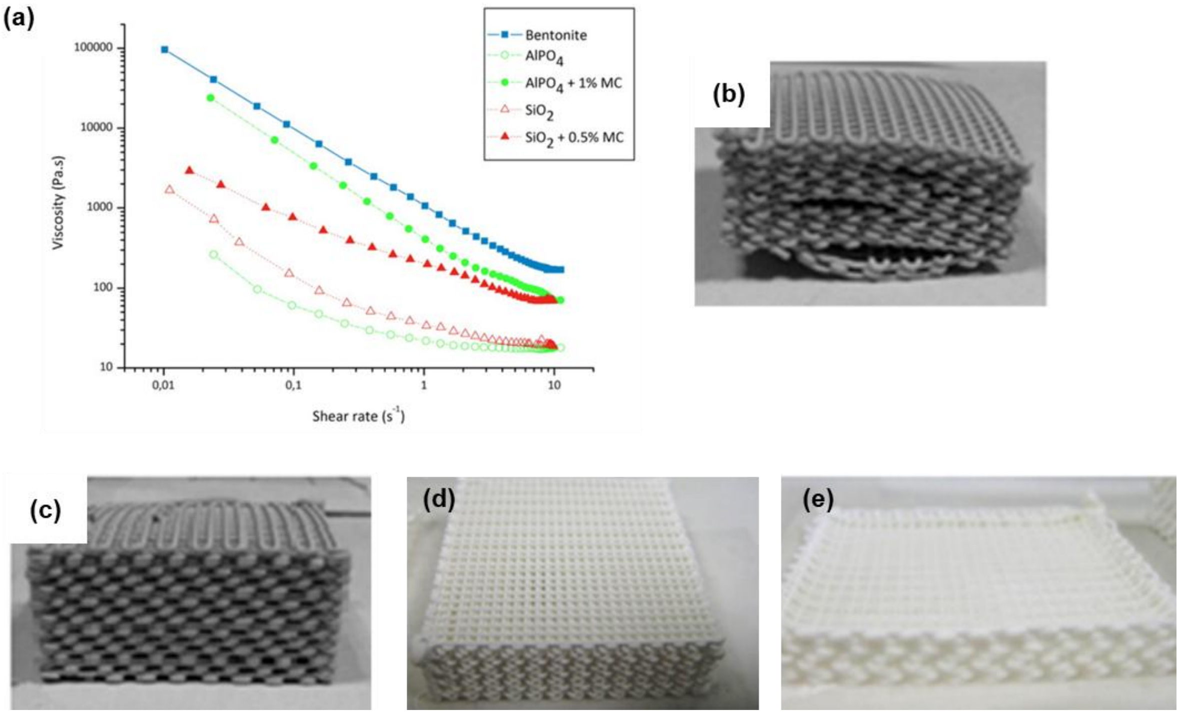

Figure 11. (a) Rheology measurements of extrusion slurries with single binder composition (bentonite after milling). MC= methylcellulose (b-c) structures containing bentonite after fast drying and slow drying in controlled atmosphere respectively (d-e) structures containing silica after fast drying and slow drying in controlled atmosphere respectively. (Reproduced from ref. 91 with permission. Copyright 2017, Elsevier.)

Table 5. Number of acid sites and crush strength of pure zeolite and different single and binary binder structures with different binder systems (65/35 zeolite/total binder weight ratio, 50/50 binders weight ratio) after calcination. (Reproduced from ref. 91 with permission. Copyright 2017, Elsevier.)

Structure	**Number of acid sites (1/Å^2)**	**Number of acid sites (μmol/g)**	**Crush strength (MPa)**
Pure H-ZSM-5	1.17	834.0	-
Bentonite	0.74	361.0	0.22 ± 0.03
Silica	0.64	322.5	0.25 ± 0.11
AlO$_4$	2.62	710.1	0.54 ± 0.16
Bentonite/AlO$_4$	1.47	533.0	1.54 ± 0.24
Bentonite/silica	0.80	401.3	0.66 ± 0.25
Silica/AlO$_4$	1.77	520.8	0.57 ± 0.17

The influence of the binder systems mentioned above was determined for methanol-to-olefin (MTO) process.[92] The combination of silica with aluminophosphate was found to exhibit excellent stability, as the conversion remained above 90% for 50 hours, nearly twice as long as that observed for pure ZSM-5 (Figure 12a). Furthermore, this binder combination exhibited high selectivity towards propylene and showed a high propylene/ethylene ratio (Figure 12b). These works highlight the benefits and drawbacks of using inorganic binders in 3D-printed monolith.

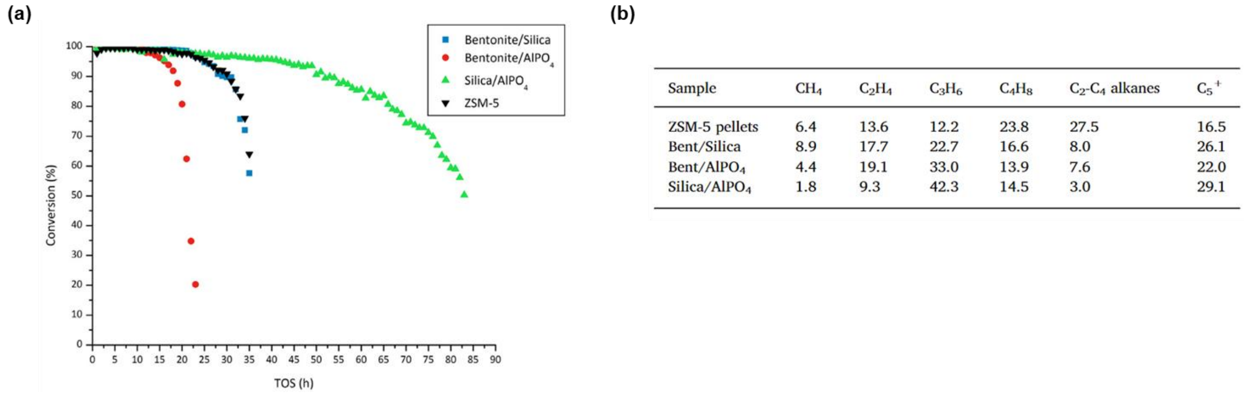

Sample	CH_4	C_2H_4	C_3H_6	C_4H_8	C_2-C_4 alkanes	C_5^+
ZSM-5 pellets	6.4	13.6	12.2	23.8	27.5	16.5
Bent/Silica	8.9	17.7	22.7	16.6	8.0	26.1
Bent/AlPO$_4$	4.4	19.1	33.0	13.9	7.6	22.0
Silica/AlPO$_4$	1.8	9.3	42.3	14.5	3.0	29.1

Figure 12. (a) methanol conversion of hydrocarbon as a function of time and (b) corresponding selectivity at 90% methanol conversion with binary binder system. (Reproduced from ref. 92 with permission. Copyright 2018, Elsevier.)

Apart from the binder, metal dopants also play an important role in the zeolitic catalysts.[93–96] Instead of using traditional doping methods such as ion-exchange or impregnation, Li and coworkers prepared 3D-printed metal doped zeolitic monolith *via* the addition of metal precursors into the printing slurry.[93] The results showed that metal dopants have an influence on the acidity, the pore size distribution, the mechanical and catalytic properties of the printed monoliths. As reported in Table 6, all investigated metal dopants (Cr, Cu, Ga, La, Mg, Y, Zn) have an effect on the textural properties of the zeolitic monolith. When the monolith is doped with Cr, Cu, Ga, Y, and Zn , the microporous volumes decreased by about 10% compared to undoped monolithic structure. It suggests that these metals barely entered the micropores of the zeolite and affected the mesopores. Furthermore, Mg-doped ZSM-5 monolith displayed significant decrease in both micropore and mesopore volumes suggesting the existence of the metal dopants in the micropores in addition to mesopores. As for the acidity, Mg and Zn doped ZSM-5 monolith possessed only weak acid sites (Figure 13a) identified by low temperature range (400-600 °C) for ammonium. This suggests that the metal dopant converted some of the strong acid sites to the weak sites by exchanging the proton on zeolite hydroxyl group, and hence moderated the acidity of the catalyst. In addition, various metal dopants, except for Cu/ZSM-5, has improved the mechanical properties of printed monoliths, resulting in higher compressive strength (Figure 13b). Ga/ZSM-5 demonstrated the highest improvement in critical compressive strength among the investigated metal dopants, reaching 4.61 MPa, which is four times higher than that of the bare ZSM-5 monolith. Finally, Mg/ZSM-5 showed the most improved ability to produce light olefin, namely C2=, C3= and BTX (benzene-toluene-xylene), in the methanol-to-olefins process (Figure 13c). Moreover, the outstanding coke resistance of this doped monolith, explained by the occupied space in micropores, helps to make 3D-printed ZSM-5 monoliths with metal incorporation promising catalysts.

Table 6. Textural properties (obtained by nitrogen physisorption) of ZSM-5 monoliths calcined at 550°C for 6h and doped with different metals. (Reproduced from ref. 93 with permission. Copyright 2018, Elsevier.)

Samples	S_{BET} (m^2/g)	S_{micro} (m^2/g)	S_{ext} (m^2/g)	V_{micro} (cm^3/g)	V_{meso} (cm^3/g)	Metal loading (wt%)
ZSM-5	373	261	168	0.100	0.200	-
Cr/ZSM-5	286	180	106	0.090	0.129	11.62

Cu/ZSM-5	297	197	100	0.096	0.106	9.56
Ga/ZSM-5	318	197	121	0.096	0.117	10.31
La/ZSM-5	335	215	120	0.105	0.129	8.95
Mg/ZSM-5	229	178	51	0.087	0.090	8.64
Y/ZSM-5	293	185	108	0.090	0.118	10.34
Zn/ZSM-5	285	185	100	0.090	0.137	11.34

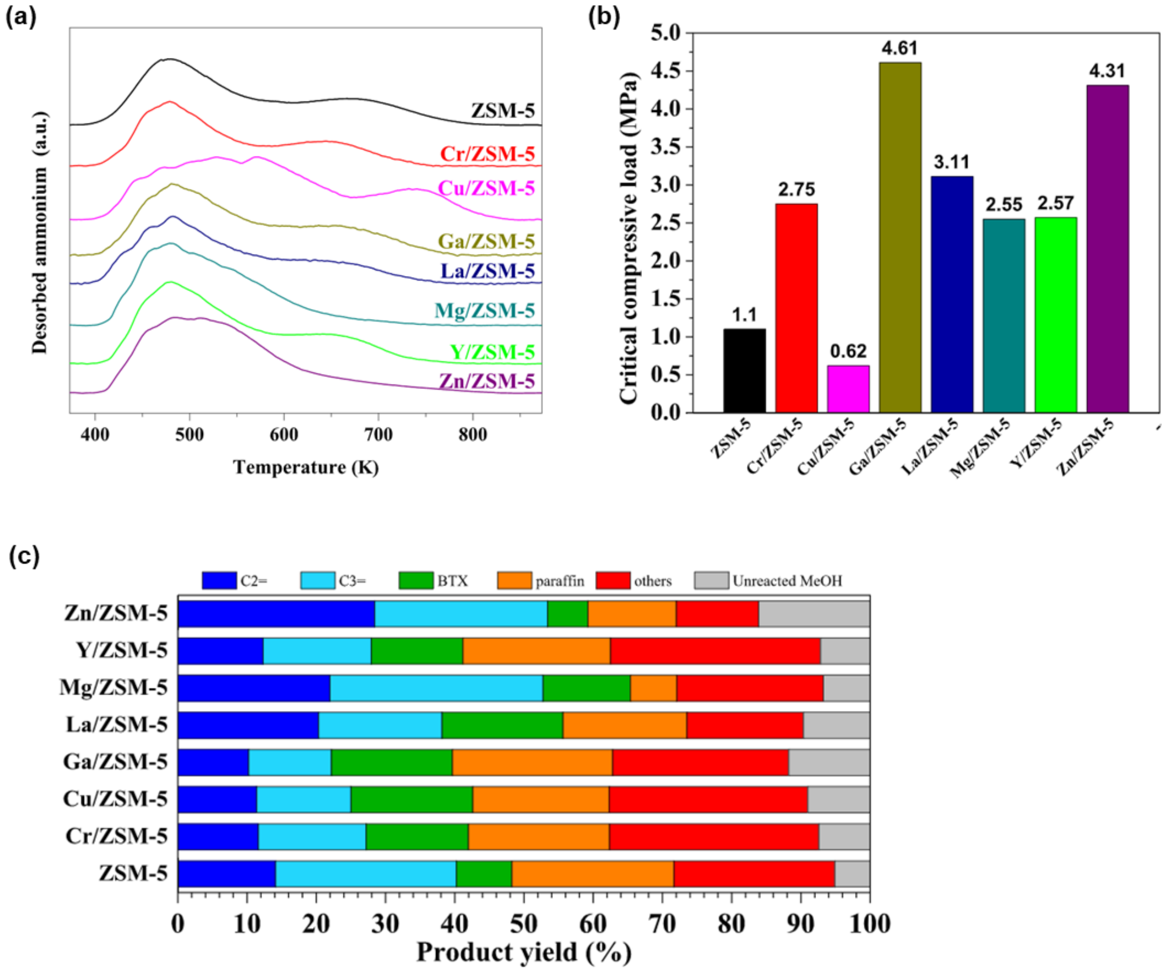

Figure 13. (a) NH_3-TPD profiles, (b) the critical compressive stress and (c) product distribution for MTO reaction for doped 3D-printed monoliths. (Reproduced from ref. 93 with permission. Copyright 2018, Elsevier.)

In general, the demand for catalysts with complex geometries has increased in recent years, so 3D printing has become a trend due to its flexibility and versatility. 3D-printed monoliths have many advantages, including robust mechanical properties, large surface areas, catalytic stability and the ability to incorporate functional binders or metal dopants.

4.1.3. 3D printing *via* extrusion for electrode manufacturing

Activated carbons are used as electrode material to store energy since they are conductive and have a large surface area. There is a rapid development in recent years of flexible energy storage devices. However, the fabrication of functional flexible electrochemical double layer capacitors (EDLCs) in one single process remains a challenge as many different types of materials being used in EDLCs. The use of 3D printing provides a novel efficient, easy and low-cost method to manufacture EDLCs. [100–102]

Areir et al. reported the printing of a highly flexible EDLC *via* FDM with the dimensions shown in Figure 14a.[100] This EDLC consists of two electrodes, a gel electrolyte as a separator, and current collector layers. The fabrication process involved a single continuous FDM printing method, as depicted in Figure 14b. Each part of the EDLC was printed by a nozzle, where the paste of the corresponding material was extruded and deposited step by step on the build platform covered with Teflon paper. Particularly, the activated carbon (AC) paste was prepared by milling the carbon into uniform size (about 0.4 μm). PVA gel solution was then used as plasticizer to adjust the rheological property. Besides, phosphoric acid (H_3PO_4) and CMC were added to ensure the homogeneity. The 3D printed EDLCs have outstanding capacitance for different combination circuits. Based on the cyclic voltammetry (CV) curves, the area specific capacitance of the flexible EDLC was calculated: it is 1.48, 0.45, and 0.13 F cm^2 at scan rates of 20, 50, and 100 mV s^{-1}, respectively (Figure 14c). The increase of the capacitance with the decrease of the scan rate may be attributed to the fact that at the lower scan rate the ions could travel deeper inside the AC material leading to a better surface coverage reaction. According to the galvanostatic charge/discharge (GCD) test at different currents (Figure 14d), the iR drop increased when the current increased. The capacitance calculated by the GCD was 4.13, 2.65,1.93, 0.45, and 0.1 F at currents of 4, 6, 8, 10, and 15 mA, respectively. The specific energy density and specific power of the printed EDLC can be calculated as 0.064 Wh kg^{-1} and 57.60 W kg^{-1}. The mechanical bending of 3D EDLC showed retention of 54–58% of its original capacitance at 50 mV s^{-1} (Figure 14e). Although the specific energy of the flexible EDLC in PVA/H_3PO_4 gel electrolytes was not comparable with organic electrolyte based EDLCs, the advantage is the unique flexibility.

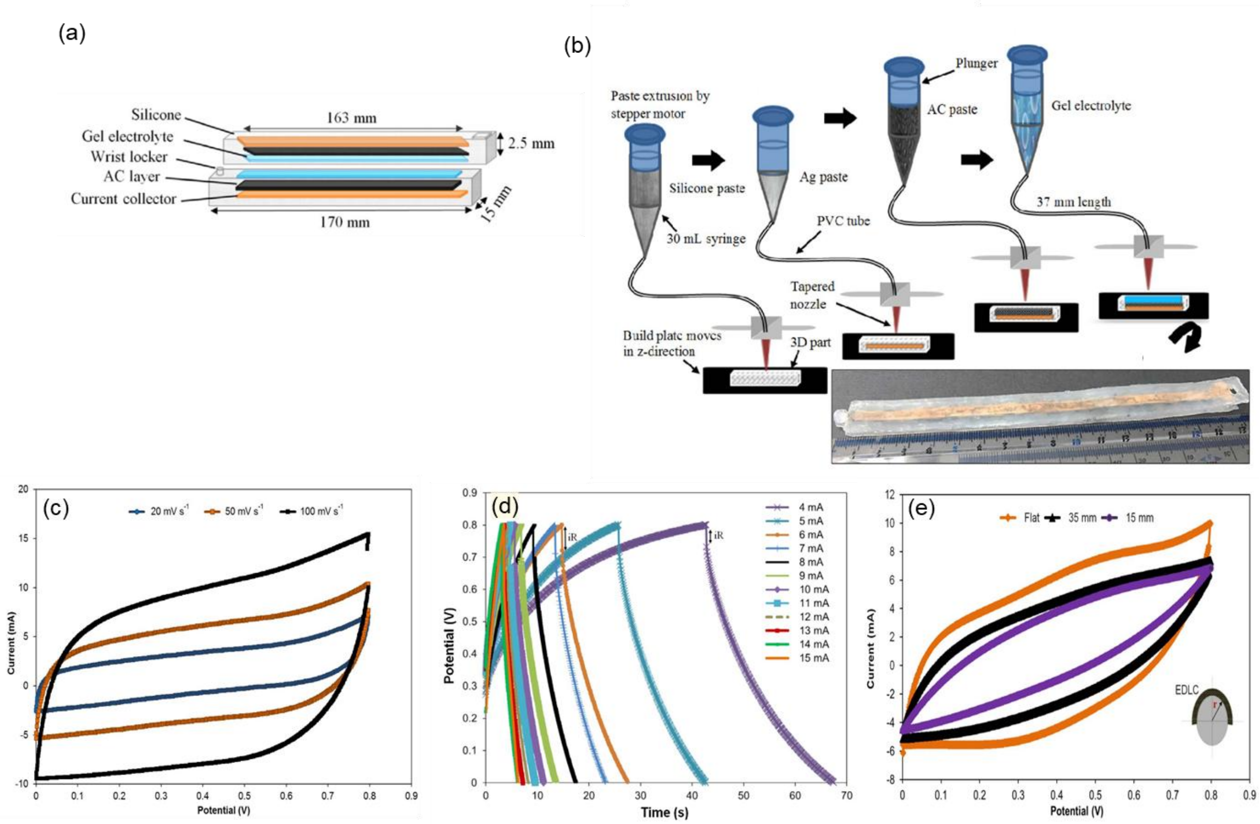

Figure 14. (a) Structure of printed EDLC (b) scheme of the 3D flexible EDLCs manufacture (c) CV curves of printed EDLC recorded at different scan rates (d) GCD curve recorded at different charge currents; (e) CV curve of 3D flexible EDLC at 50 mV s^{-1} under flat (170 mm), bent radius of 35- and 15-mm conditions. (Reproduced from ref. 100 with permission. Copyright 2017, Elsevier.)

Lyu et al. reported a 3D-printed cathode by embedding cobalt-based MOF in an organic binder (Pluronic F127).[103] As a result, the practical specific energy for Li–O_2 batteries was effectively increased to 798 Wh kg^{-1}_{cell}. In another study, a magnetic COF and bovine serum albumin (BSA) were co-deposited on the surface of 3D-printed nanocarbon electrode to manufacture chiral biosensors.[104] The electron transfer efficiency and the selectivity towards tryptophan enantiomers were reported to be improved. Other researchers have reported the fabrication of CNTs or graphene-based supercapacitors *via* direct-ink writing[105–111], micro extrusion[112,113] and FDM [114–117].

4.1.4. Challenges and outlooks for extrusion 3D printing

Based on the research carried over the last 5 years, Direct Ink Write (DIW) is currently the most developed technique. It allows for the tuning of scaffold geometry and printing of various porous materials. Various porous solids including zeolites, aminosilica, MOFs and COFs can be employed as active materials and manufactured into desired structures through DIW. However, there exists some challenges that need to be addressed for this printing technology to compete with traditional manufacturing methods. First is that the ability to formulate binderless monoliths or pellets is not well established. Permanent binders such as bentonite and silica are commonly used in zeolitic monoliths, particularly for adsorption or catalytic applications. In the case of MOFs and COFs, the polymer matrix is typically retained after the printing process, as they are unable to withstand the high temperatures required for the removal of the polymer through thermal treatment. Further advancements are needed in this area to enhance the versatility of 3D-printed adsorbents and catalysts. The second challenge lies in the optimization of the slurry Printing with large particles can give rise to problems such as solvent evaporation and tip blockage, rendering the slurry non-printable. Rheological optimization is often a trial-and-error procedure that relies on manual intervention. Therefore, it is crucial to develop automated methods for ink optimization. Automation of the 3D printing process remains another challenge as there are currently few fully automated systems that can simultaneously evaluate and adjust multiple parameters. To streamline the printing process and enable industrial-scale production, advancements in optics, robotics, process control, and machine learning are necessary. Finally, comprehensive economic studies are needed to compare this 3D printing technology with established technologies in terms of costs, output, and return on investment. These analyses would provide insights into the competitiveness of 3D printing in relation to traditional manufacturing approaches.

In conclusion, the future of adsorbents and catalysts fabrication through extrusion 3D printing lies in overcoming the challenges related to manufacturing protocols, slurry optimization, geometric design, automation, and economic analysis. By addressing these limitations, DIW has the potential to become a viable alternative to traditional manufacturing methods.

4.2. 3D printing *via* photopolymerization

4.2.1. Recent advances in 3D printing of porous materials *via* photopolymerization

Table 7 summarizes recent publications that use photopolymerization to produce structured monoliths of porous materials. Active materials such as zeolites or MOFs can be directly introduced into a photosensitive resin, allowing shaping under the irradiation at a specific wavelength.[114-119, 120] For instance, O. Halevi et al. fabricated polymer-based composites with zeolite as filler for Sr^{2+} and Cs^{+} uptake in nuclear wastewater.[118] 25 wt% of LTA 4A or chabazite zeolites were mixed with acrylate resin which was then printed by DLP. The printed polymer-based composite allows ion exchange in aqueous medium. Similarly, Merilaita et al. fabricated for the first time polymer based composite with MFI zeolite *via* SLA.[119] The zeolite content in the printing slurry can achieve 55 vol% and the viscosity of slurry was reduced to ca. 7 Pa s with 2.5 wt% of a dispersing agent (BYK-180).

In recent works realized by our team, the LTA-5A and FAU-13X zeolites content has reached 95 wt% with a formulation containing PEGDA, BDMK and a solvent (toluene).[120] As illustrated in Figure 15a and b for LTA-5A content of 80%, the shaping is preserved during the calcination up to 700 °C (Figure 15a), and the textural properties are comparable to those of the pristine powder (Figure 15b). LTA calcined composites are potentially interesting for CO_2 adsorption as the uptake ($p/p^0 = 0.030$) is only 6.2 % lower than that of powder but 23 % higher than that of some commercial beads (Figure 15c). Moreover, calcined composites possess high enough water gas adsorption rates to consider them as dessicants since their adsorption capacity at RH = 50% is 21.6 wt% and 23.2 wt% for LTA (Figure 15d) and FAU respectively.

Inorganic binders such as Al_2O_3[121] and SiO_2[122] were investigated to improve the mechanical property of zeolitic monolith and to introduce hierarchical porosity after calcination for different applications. More details are provided in Table 7.

Active material and content	**PI**	**Monomers**	**Technique**	**Post treatments**	**Applications and capacity**	**notes**	**ref**
Ordered Mesoporous Silica	TPO	epoxy acrylate, urethane diacrylate	DLP (385 nm, 30 mW/cm^2)	calcined at 700 °C, shrinkage: 61. 8 vol%	catalysis, separation, drug delivery, etc. (S_{BET} = 1900±80 m^2/g)	3D printing of a precursor solution containing structure-directing agent, silica and monomers	130
(K, Na)-CHA, LTA 4A 25 wt% (45-50% after solidification)	TPO	Ethoxylated bisphenol A diacrylate, dipropylene glycol diacrylate	DLP (405 nm, 39 mW/cm^2)	solvent exchange in absolute ethanol	Sr^{2+} and Cs^+ uptake (CHA: 24.3% for Cs^+, 6.6% for Sr^{2+}; LTA: 18.5% for Cs^+ and 5.2% for Sr^{2+})	porogenic solvent enabled the formation of pores on polymer and contribute to ion diffusion	118
LTA 5A (Macklin) 21 wt%	BAPO	polyether acrylate	DLP (405 nm)	calcined at 650 °C	CO_2 adsorption: 25 °C 0.6 MPa (1.6 mmol/g)	bentonite was used as binder to improve mechanical properties with zeolite/binder ratio: 70/30	131
Cu-BTC 10 wt%	BAPO, HCPK	2-phenoxyethyl acrylate, PEGDA	DLP (405 nm, 41 mW/cm^2)	heated up to 250 °C where polymer weight loss achieves 30–40 wt%	MB removal (0.7 mg/g)	printed Cu-BTC@polymer could avoid the hydrolysis and the absorbed MB being released back to solution	124
LTA 5A and FAU 13X up to 95 wt%	BDMK	PEGDA	LED lamp (405 nm, 1 W/cm^2)	thermal treatment at 600 and 700 °C respectively for 30 min	CO_2 adsorption: 0 °C, p/p0=0.03 (107/114 cm^3/g^{-1} for LTA/FAU) water uptake: RH = 50% (26.1/30.3 wt% for LTA/ FAU)	toluene was selected as solvent	120
LTA 5A (Al_2O_3 as binder) 50 wt% in total	BDMK	PEGDA, TMPTA, HDDA	LED lamp (405 nm, 1 W/cm^2)	calcined at 750 °C for 4h	CO_2 adsorption: 0 °C, p/p0=0.03 (2.7-4.3 mmol/g)	using Al_2O_3 as binder improved the mechanical property of calcined composite but reduced S_{BET}	121
LTA 5A (colloidal silica as binder) up to 52 wt%	BDMK	PEGDA	LED lamp (405 nm, 1 W/cm^2)	calcined at 600°C for 30 min	Sr^{2+} and Ni^{2+} uptake (22% for Sr^{2+}, 8% for Ni^{2+})	silica particles introduce hierarchical porosity and improve the mechanical property of printed monolith	122
Ag modified halloysite 1-3 wt%	TPO	UMDA, TEDGMA	DLP (405 nm)	-	antibacterial dental composites	improvement of flexural properties thanks to the addition of halloysite	132
MFI (ZSM-5 zeolite) 55 vol%	N/S	acrylate and epoxy	SLA (460 nm 39.36 mW/cm^2)	calcined at 500 °C	gas adsorption (S_{BET} = 311 m^2/g)	printing layer thickness=50 µm	119
UiO-66	BAPO	TMPPTA, BECRYL® 8413	LED lamp (365 nm	heated to 280 °C and wash with DCM	methyl paraoxon to dimethyl phosphate (conversion ~100%)	irradiated with 365 nm UV light during printing	123
$Zr_6O_4(OH)_4$-MMA	TPO	MMA ligands	DLP (385 nm, 10 mW/cm^2)	solvent exchange and freeze drying	CO_2 adsorption: 30 °C 0.1MPa, N_2:CO_2 = 80:20 (1.92 wt%)	photoresponsive ligand on inorganic core. MMA can act as a molecular connection by photopolymerization and offer colloidal stability	128
$[Ni(AAm)_4(-H_2O)_2](NO_3)_2$	TPO	acrylamide ligands	DLP (405 nm)	exposed to UV-light for 5 min, washed with absolute ethanol and dried under vacuum	S_{BET} = 53.32 ± 23.00 m^2/g	open the path-ways for various applications that require complex architectures	127

Table 7. List of monoliths fabricated through photopolymerization

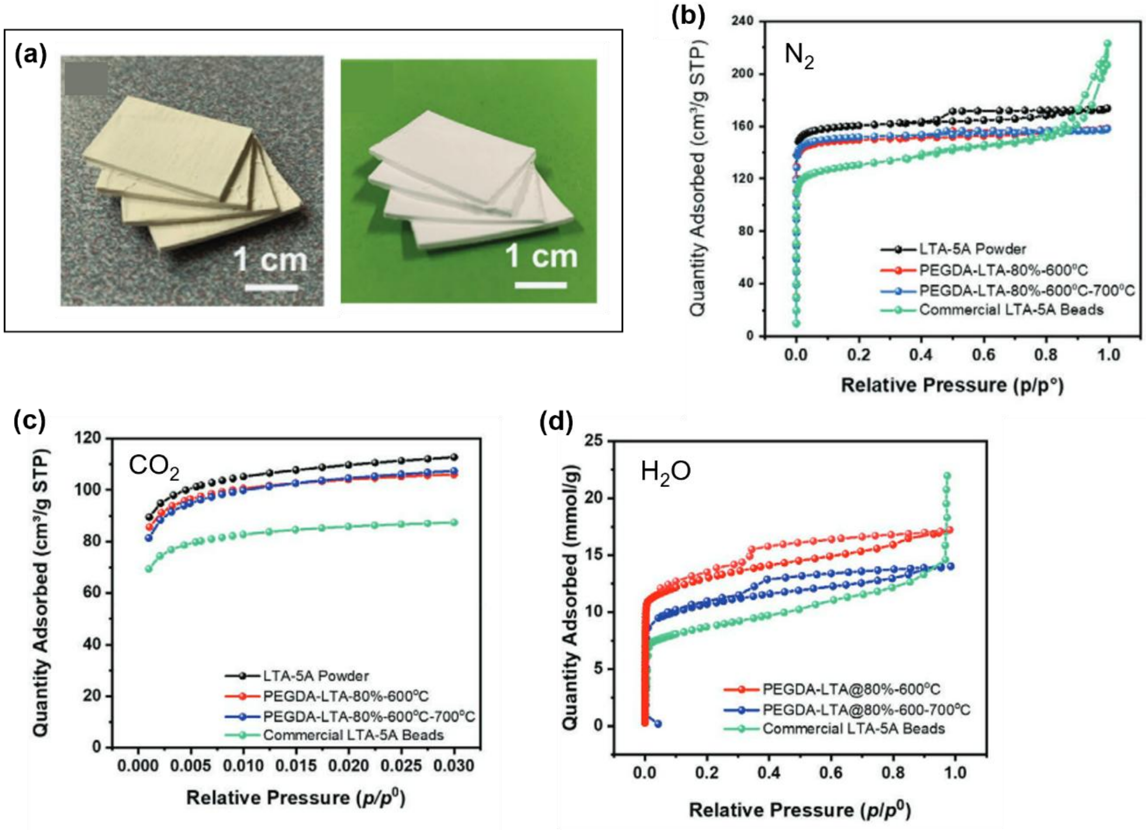

Figure 15. (a) 3D structure objects of polymer-zeolite composite (80 wt% of LTA in PEGDA) before (left) and after (right) calcination at 700 °*C*; (b-d) N_2, CO_2 and H_2O isotherms for pristine zeolite powder, calcined monolith and commercial beads respectively. (Reproduced from ref. 120 with permission. Copyright 2021, Wiley.)

Apart from zeolites, MOFs can also be prepared in the same way. Young et al. prepared a photopolymerizable printing paste containing pre-synthesized UiO-66 to fabricate shaped catalyst.[123] 52 wt% UiO-66 was generally added to a mixture of photoinitiators with two different acrylates. This paste displayed shear-thinning property (Figure 16a) which was suitable for DIW process. After post thermal treatment at 280 °C and rehydration, the printed MOF monolith showed comparable catalytic properties to those of the MOF powder in the cracking reaction of methyl paraoxon (Figure 16b). In another work, 10 wt% of Cu-BTC was incorporated in acrylate resin and printed by DLP.[124] This printing process improved significantly the hydrolytic stability of MOF powder and allowed efficient MB adsorption in aqueous solution during a long period.

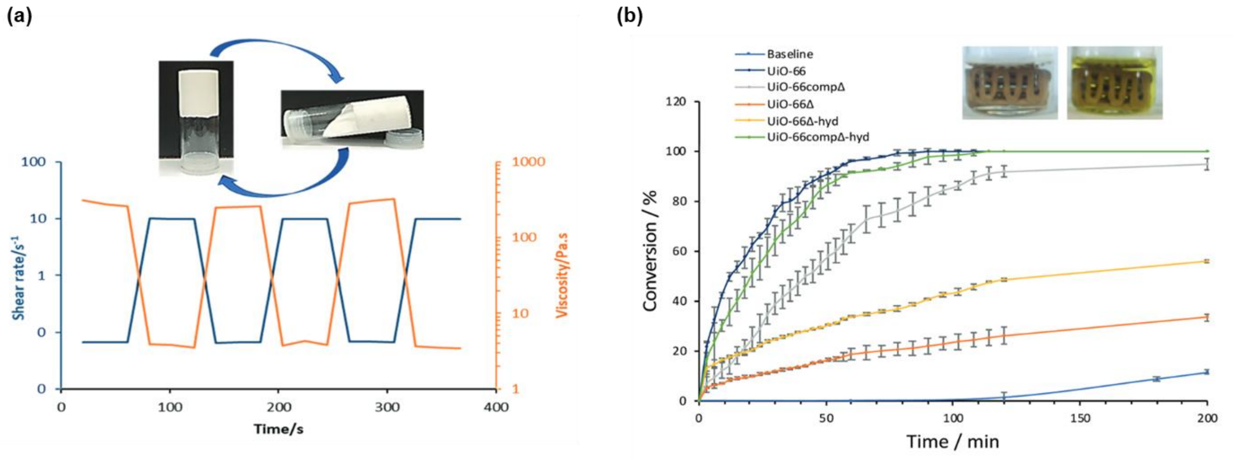

Figure 16. (a) Rheological behavior of UiO-66 composite ink, simulating the extrusion process at the nozzle (non-continuous extrusion when printing) (b) conversion of methyl paraoxon to dimethyl phosphate. Inset: Photographs of UiO-66 composite in a reaction mixture at the start of the reaction (left) and after 200 minutes (right). (Reproduced from ref. 123 with permission. Copyright 2019, Royal Society of Chemistry.)

However, adding fillers to the photopolymerizable resin will induce light penetration issue. The optical loss mainly comes from the light absorption and scattering of the filler particles and the mismatch of refractive indexes between filler and resin.[64,125] The optical properties of filled system determine not only their aesthetic appearance but also their curing depth and polymerization kinetics.[126] Furthermore, the incorporation of porous materials in polymer matrix blocks their pores and reduces their accessible surface area, which strongly limits their applications. Porous coordination polymers (PCPs) have drawn the attention of researchers in recent years as one of the potential solutions to the aforementioned issues. The ligands linked to the cationic center can be tailored with functional groups (acrylates or acrylamides for example) which allow polymerization. The self-standing material after polymerization exhibits huge porosity and can be potentially applied in various domains. In the prior work of O. Halevi et al., a metal-containing-monomer (NiComplex) based on nickel ion and acrylamide ligands, $[Ni(AAm)_4(H_2O)_2](NO_3)_2$ was printed with the presence of a photo initiator *via* DLP (Figure 17).[127] This printed material has a mesoporous structure with surface area of 53.32 ± 23.00 m^2/g.

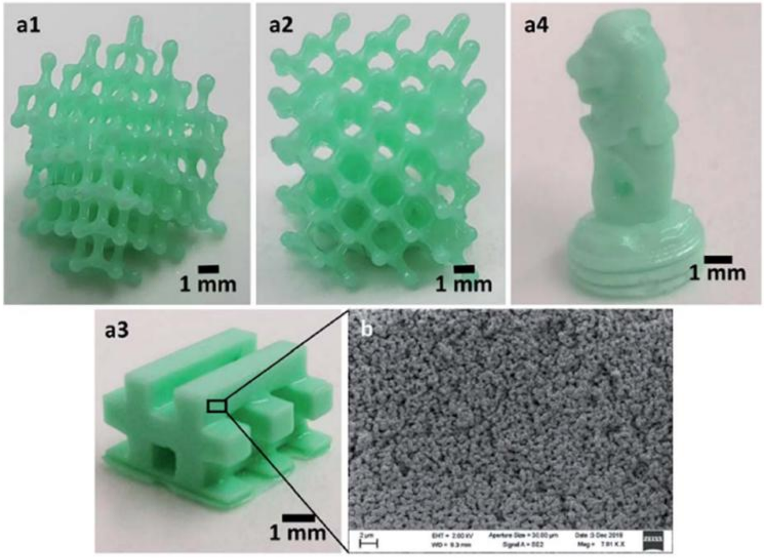

Figure 17. (a1-a4) 3D-printed structures of polyNiComplex, (b) cross-section of the printed polyNiComplex (Reproduced from ref. 127 with permission. Copyright 2020, Royal Society of Chemistry.)

In another work of Huang et al., a Zr based complex functionalized with methacrylic acid ligands was printed using the same method.[128] The printed material exhibits hierarchical structure and presents high BET surface area of 679 m^2/g. The results also suggested that the print speed and drying method (solvent removal) can have an influence of the pore size distribution. CO_2 adsorption capacity of the printed Zr complex is comparable to the Zr-based MOF UiO-66.[129]

4.2.2. Challenges and outlooks for 3D printing *via* photopolymerization

In recent years, photopolymerization-based 3D printing has seen rapid development in the production of ceramic parts such as Al_2O_3, ZrO_2, SiC, and others. This technology has reached a relatively mature stage in this field. However, there have been limited works or publications utilizing the same technique to fabricate monoliths of porous materials (Zeolites, MOFs, COFs…). The main obstacles for this printing method to be scaled-up for industry production can be summarized as follows:

- Difficulty to produce polymer-free porous monoliths. The use of photopolymers is essential in this printing technique, but removing the polymer component to achieve porosity for applications like adsorption or catalysis is a tricky issue. Unlike ceramics, which can withstand high temperatures exceeding 1000 °C and be densified to achieve robust mechanical properties, porous materials, including most zeolites, tend to collapse at such temperatures. Lower temperature used to calcine zeolite/polymer composites usually results in unsatisfied mechanical characteristics. For MOFs, the printed composites typically undergo a thermal treatment below 300 °C.[123,124] However, this temperature range is insufficient for the complete removal of the polymer component.

- When using zeolites or MOFs as filler, the light scattering arising from the solid particles results in poor light penetration and undesirable broadening of the curing area. There is lack in discussion of the printing resolution as well.
- Compromise between material loading and printability of the printing slurry. It is preferred to have a higher solid loading for better shape retention after calcination, as well as improved mechanical properties. However, higher solid loading results in reduced fluidity and printability as well as poor light penetration.

To address the aforementioned challenges, improvements are needed in various aspects of photopolymerization-based 3D printing. Firstly, printer devices need to be enhanced to accommodate formulations with higher filler content and higher viscosity. For instance, the combination of extrusion-based printing and photopolymerization can be employed, where materials are deposited layer by layer onto the build platform for sequential curing, or simultaneous extrusion and curing can be implemented. Alternatively, printing of precursors can be explored as a means to circumvent the challenges associated with fillers and high viscosity. Significant research has been conducted in ceramic printing using this approach, demonstrating promising results, while in the field of porous materials, there have been relatively few reports.[130] Advancements are needed in optimizing precursor formulations, exploring different materials, and evaluating structural properties and performance. Secondly, one of the advantages of photopolymerization is the versatility in choosing light sources, particularly the rapidly advancing LED curing technology. LEDs offer high luminous efficiency, with flexible wavelength design options. Additionally, they are energy-efficient, generate minimal heat, do not produce ozone, and require no solvents, making them environmentally friendly. In comparison to traditional shaping methods of porous material, LED curing demonstrate significant advantages. However, there is a limited availability of commercially viable photoinitiators specifically developed for LED light sources, particularly for formulations with high filler content. Further research and development are necessary in this area. Lastly, more research and data are required to advance printing accuracy. Comprehensive studies on print resolution, dimensional accuracy, surface quality, and mechanical properties of printed porous structures are essential to establish reliable guidelines and standards for 3D printing in this domain. These efforts will contribute to the refinement and wider adoption of 3D printing techniques for porous material fabrication.

4.3. 3D printing *via* powder-based technologies

Due to the restriction of temperature, powder bed 3D printing technologies are less represented involving porous materials. Some researchers reported the printing of MOFs together with selected polymers *via* SLS, as MOFs alone would not withstand the high temperature. The polymers that can be employed are polyamide 11 or 12 (PA11/PA12), thermoplastic elastomers (TPEs) and thermoplastic polyurethane (TPU).[55]

Lahtinen et al. reported the printing of MOF-polymer composite *via* SLS for CO_2 capture (Figure 18).[58] 10 wt% of HKUST-1 was mixed with PA12 without any pretreatment and the printing process was operating at 170 °C. As a result of the selected printing conditions, HKUST-1 was strongly bonded to the surface of the partially fused polymer particles, retaining its particle-like structure and high porosity. The structural stability was confirmed by X-ray diffraction (XRD) analysis and CO_2 adsorption tests before and after printing. The MOF powder and composite adsorbed up to 6 and 0.6 wt% CO_2 respectively which is perfectly in agreement with the composition of the 3D printed object which contains 10 wt% of the active MOF.

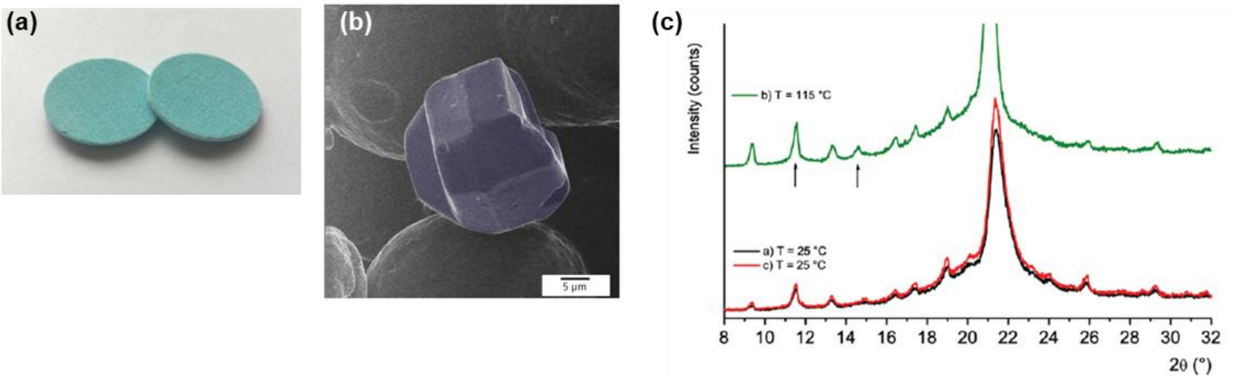

Figure 18. (a) 3D printed MOF/PA 12 disks with 20 mm diameter and 1.5 mm thickness (b) Helium Ion Microscopy (HIM) image of the surface of printed disk (c) powder XRD patterns MOF/PA12 recorded at 25°C, 115 °C and after cooling to 25 °C. (Reproduced from ref. 58 with permission. Copyright 2019, Wiley.)

In another work, Chen et al. demonstrated the possibility of *in-situ* synthesis of ZIF-67 on the surface of PA12 (Figure 19a), which was subsequently laser sintered to fabricate porous structures with additional macro-pores and controlled cavities to increase the surface area.[59] The as-synthesized nanocomposites contain 0.1 to 2 wt% of ZIF-67 into PA12 powder, and a negligible influence on the particle size distribution compared to PA12 before synthesis is then observed (Figure 19c). The surface area increases from 12.1 m^2/g (pure PA12) to 68.2 m^2/g in the presence of 2% ZIF-67. Both solid structure and porous structure were designed and printed in order to study the influence of monolith's structure on CO_2 uptake (Figure 19b and d). The results show that the monolith loaded to 2% with ZIF-67 with porous structure adsorbed most efficiently: 3.02 and 4.89 cm^3/g at 298 and 273 K (1 bar) respectively. This is significantly higher proportion than its MOF loading, as the ZIF-67 powder adsorbed 20.1 and 32.3 cm^3/g of CO_2 under the same conditions. This result on adsorption capacity exceeds those obtained in the previous study of Lahtinen, where the MOF powder was simply mixed with PA12.[58] The study of Chen et al. demonstrates the unique advantage of *in-situ* synthesis of MOF/polymer composite for SLS 3D printing.

Other MOFs like NH_2-MIL101(Al), ZIF-8 and MOF-801 can also be printed by SLS (106 nm) with weight loadings from 10-40 wt% in PA12.[133] The printed composites (films) were tested for MB adsorption in aqueous solutions. NH_2-MIL101(Al)-PA12 with grid pattern showed the most satisfactory adsorption capacity and rate among the printed MOFs. In addition, the film can be directly regenerated in methanol for reuse.

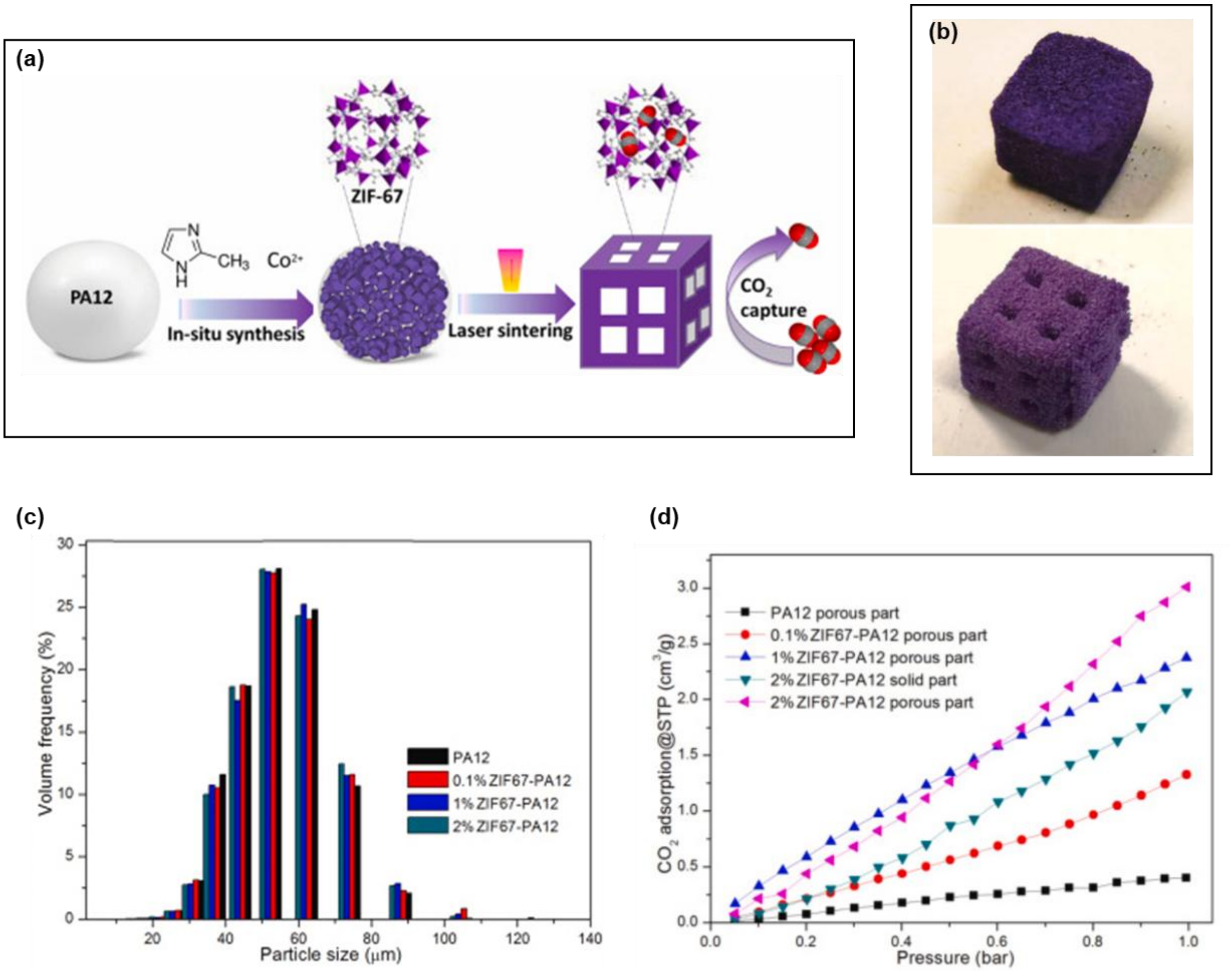

Figure 19. (a) Scheme of *in-situ* synthesis way of ZIF-67/PA12 composite and monoliths preparation *via* SLS (b) printed monoliths with solid structure (above) and porous structure (below) (c) particle size distribution of PA12 and as-synthesized MOF/polymer with different MOF loadings (d) CO_2 adsorption by different monoliths at 298 K and 1 Bar. (Reproduced from ref. 59 with permission. Copyright 2020, Elsevier.)

Azhari et al. reported for the first time the fabrication of graphene-based electrodes for high performance supercapacitors by binder-jet powder bed technology.[134] As illustrated in Figure 20a, a liquid binder consisting of 90% water, 8% glycerol and 2% other humectants was injected on a layer of thermally reduced graphene oxide (TRGO) powder with controlled thickness (100 μm in the study) to create desired shape. Then a rotating roller moved pushing a layer of powder from the feed bed to cover the build bed. The binder jetting was repeated layer by layer to create the final 3D structure. As the synthesized TRGO has an extremely low bulk density (i.e. $\sim 10^{-2}$ g cm^{-3}), the flowability of the powder must be enhanced by mixing with acetone which is then evaporated before the printing process. The bulk density is increased after this, thanks to the capillary consolidation. As shown in Figure 20b, the lateral resolution is limited to approximately 1 mm mainly due to the penetration of binder to the adjacent particles. The vertical resolution (z direction) mainly depends on the maximum particle size and on the flowability of the powder. The further impregnation with palladium nanoparticles was able to decrease the contact resistance between powder agglomerates and to improve electronic conduction, resulting in increasing the gravimetric and areal capacitance (260 F g^{-1} and 700 mF cm^{-2} respectively).

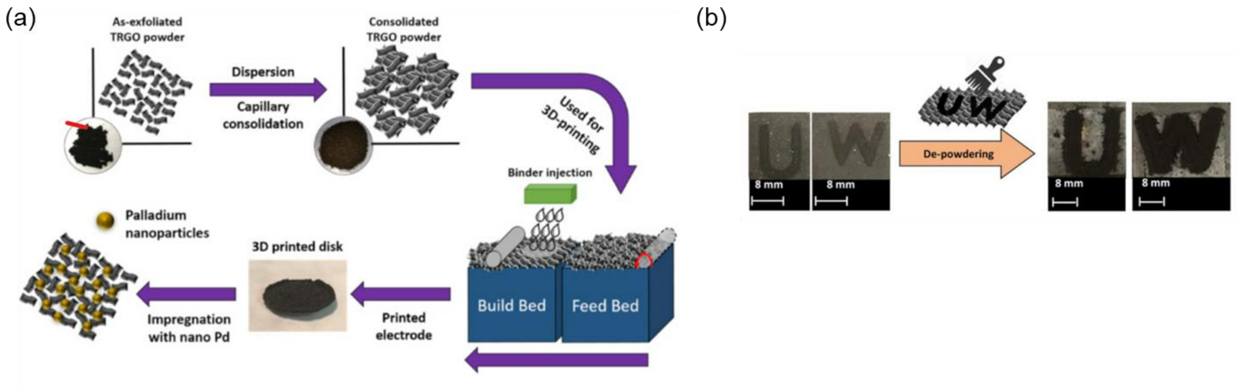

Figure 20. (a) Schematic presentation of the binder-jetting powder-bed AM technique (b) 3D printed patterns, left: patterns after printing and surrounded by the loose TRGO powder; right: patterns after removing the loose powder (i.e., de-powdering) from the printed shapes. (Reproduced from ref. 134 with permission. Copyright 2017, Elsevier.)

Shen et al. then prepared electrically conductive GO/PVOH (graphene oxide/polyvinyl alcohol) composites with high flexibility *via* binder-jetting.[137] Instead of using graphene flakes (0.5-5 μm) as powder bed, they dispersed 0.5 mg mL^{-1} graphene flakes in water together with 0.03 vol% surfactant. Then this aqueous ink was used to print a continuous line over PVOH powder. To enhance flexibility, the resulting GO/PVOH composites underwent treatments in a glycerol bath (as a plasticizer) and distilled water bath, followed by drying on a 40 °C hot plate. The authors also explored various reduction procedures for the printed electrode to partially restore the graphene structure to produce reduced graphene oxide. Notably, the use of hydroiodic acid treatment resulted in a moderate conductivity of 0.0925 Sm^{-1}, which is remarkable for low-loading graphene/polymer composites (<0.5%). Furthermore, this treatment produced a highly compliant material with a tensile modulus of 3.59 MPa, comparable to that observed for silicone rubbers. This work is promising for the fabrication and commercialization of thick, porous graphene-based devices: it paves the way for new possibilities in this field.

So far, the application of powder-bed 3D printing technology in the fabrication of monoliths of porous materials is relatively limited, with a small selection of available materials. The main limitation of SLS comes from the high temperature induced by the laser that may potentially damage the porous material. On the other hand, the requirement to use a polymer as a binding agent in the manufacture of MOF-based monoliths results in a limitation of material loading. Regarding the binder-jet process, the lateral resolution is constrained by the size of the injection nozzle and the penetration of liquid binder to the adjacent particles. There is still a lack of in-depth research regarding the selection of binders, their adhesive properties, and the mechanical strength of the printed monoliths. Despite the small amount of porous materials in 3D printed materials, powder bed technologies give a new path for producing porous structures for application such as organic dye adsorption or electrode fabrication.

5. Conclusion and perspectives

There is great interest in the development of a wide range of technical and functional porous materials with complex morphologies and fine features for academic and industrial applications. In this review, we have mainly discussed the direct 3D printing techniques, including robocasting, photopolymerization, powder-bed technologies for zeolites, MOFs,COFs and carbon-based materials. Figure 21 provides an overview of the relevant additive manufacturing processes based on different porous materials discussed in this review: areas of application are also specified. Other approaches, such as secondary growth, surface deposition or chemical functionalization of 3D-printed scaffolds, are also possible, as Lawson et al. outline in detail.[135]

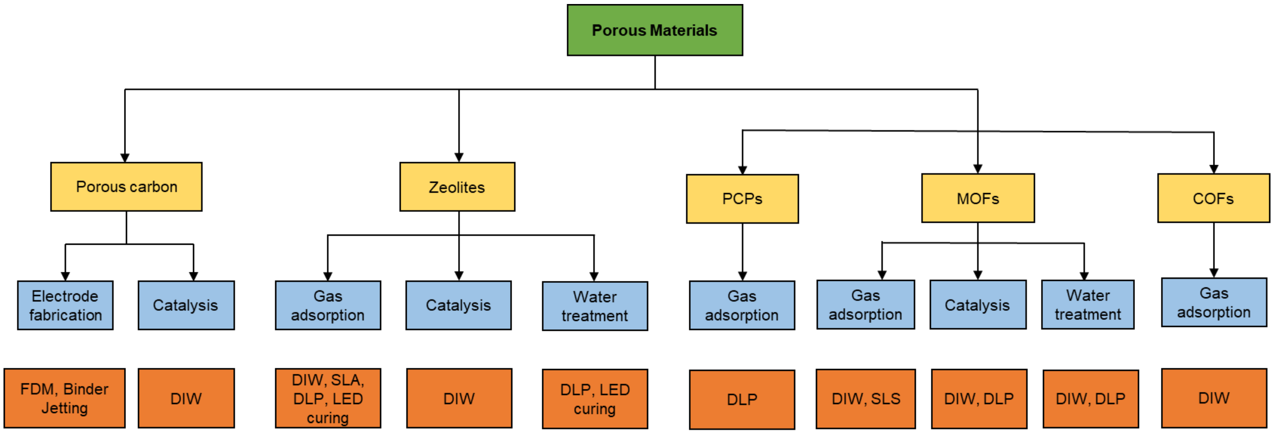

Figure 21. An overview of the relevant additive manufacturing processes based on different porous materials and their respective applications discussed in this review.

Researchers and developers working in the field of additive manufacturing now have access to an exciting new frontier thanks to the interesting combination of porous materials and versatile AM technologies. With respect to updating the production of porous monoliths, trade-offs must be made between (i) material loading, (ii) debinding, (iii) mechanical resistance of the printed structure and (iv) resolution. We believe that once the initial progress on these barriers are revealed, there will be a significant increase in the amount of knowledge associated with these concerns. This will make it easy to create a wide range of objects of various shapes and sizes. 3-D printed adsorbents will therefore become the future industrial adsorbents.

Reference

1 B. L. Huang, Z. Ni, A. Millward, A. J. H. McGaughey, C. Uher, M. Kaviany, O. Yaghi, *Int. J. Heat Mass Transf*. 2007, **50**, 405–411.

2 J. Čejka, G. Centi, J. Perez-Pariente, W. J. Roth, *Catal. Today* 2012, **179**, 2–15.

3 M. Hong, L. Yu, Y. Wang, J. Zhang, Z. Chen, L. Dong, Q. Zan and R. Li, *Chem. Eng. J.*, 2019, **359**, 363–372.

4 S. Wang, Y. Peng, *Chem. Eng. J.* 2010, **156**, 11–24.

5 E. Kianfar, S. Hajimirzaee, S. mousavian, A. S. Mehr, *Microchem. J*. 2020, **156**, 104822

6 A. Palčić, V. Valtchev, *Appl. Cata. A: Gen*. 2020, **606**, 117795.

7 S. Kesraoui-Ouki, C. R. Cheeseman, R. Perry, *J. Chem. Technol. Biotechnol*. 1994, **59**, 121–126.

8 P. Sharma, M. H. Han, C. H. Cho, *J. Nanomater.* 2016, **16**, 405-405.

9 Database of Zeolite Structures, http://www.iza-structure.org/databases/, (accessed 4 August 2022).

10 M. Hong, L. Yu, Y. Wang, J. Zhang, Z. Chen, L. Dong, Q. Zan, R. Li, *Chem. Eng. J.* 2019, **359**, 363–372.

11 Q. Meng, H. Chen, J. Lin, Z. Lin, J. Sun, *J. Environ. Sci*. 2017, **56**, 254–262.

12 K. Kawahara, K. Tsuruda, M. Morishita, M. Uchida, *Dent. Mater. J.* 2000, **16**, 452–455.

13 Ralph T. Yang, *Adsorbents: fundamentals and applications*. John Wiley & Sons, 2003.

14 A. Huang, N. Wang, J. Caro, *Micropor. Mesopor. Mater*. 2012, **164**, 294–301.

15 Z. Wu, S. Goel, M. Choi, E. Iglesia, *J. Catal*. 2014, **311**, 458–468.

16 S. Auerbach, K.A. Carrado, P.K. Dutta, K. Prabir, *Handbook of Zeolite Science and Technology*, CRC press, New York, 2003.

17 Y. Zhao, Z. Song, X. Li, Q. Sun, N. Cheng, S. Lawes, X. Sun, *Energy Storage Mater*. 2016, **2**, 35-62.

18 O. K. Farha, I. Eryazici, N. C. Jeong, B. G. Hauser, C. E. Wilmer, A. A. Sarjeant, R. Q. Snurr, S. T. Nguyen, A. Ö. Yazaydin, J. T. Hupp, *J. Am. Chem. Soc*. 2012, **134**, 15016–15021.

19 I. Ahmed, S. H. Jhung, *Chem. Eng. J*. 2017, **310**, 197–215.

20 A. A. Adeyemo, I. O. Adeoye, O. S. Bello, *Toxicol. Environ. Chem*. 2012, **94**, 1846–1863.

21 P. Kumar, A. Deep, K. H. Kim, *Trends Anal. Chem*. 2015, **73**, 39–53.

22 A. G. Slater, A. I. Cooper, *Science* 2015, **348**, aaa8075.

23 X. Feng, X. Ding, D. Jiang, *Chem. Soc. Rev*. 2012, **41**, 6010–6022.

24 A. R. Mohamed, M. Mohammadi, G. N. Darzi, *Renewable Sustainable Energy Rev*. 2010, **14**, 1591–1599.

25 M. G. Plaza, C. Pevida, B. Arias, J. Fermoso, M. D. Casal, C. F. Martín, F. Rubiera, J. J. Pis, *Fuel* 2009, **88**, 2442–2447.

26 F. Cheng, X. Yang, S. Zhang, W. Lu, *J. Power Sources* 2020, **450**, 227678.

27 G. Zhang, Y. Chen, Y. Chen, H. Guo, *Mater. Res. Bull*. 2018, **102**, 391–398.

28 P. Ozpinar, C. Dogan, H. Demiral, U. Morali, S. Erol, C. Samdan, D. Yildiz, I. Demiral, *Renew. Energ*y 2022, **189**, 535–548.

29 M. S. Shafeeyan, W. M. A. W. Daud, A. Houshm, A. Shamiri, *J. Anal. Appl. Pyrolysis* 2010, **89**, 143–151.

30 A. P. Côté, A. I. Benin, N. W. Ockwig, M. O'Keeffe, A. J. Matzger, O. M. Yaghi, *Science* 2005, **310**, 1166–1170.

31 F. J. Uribe-Romo, J. R. Hunt, H. Furukawa, C. Klöck, M. O'Keeffe, O. M. Yaghi, *J. Am. Chem. Soc*. 2009, **131**, 4570–4571.

32 G. T. Whiting, A. D. Chowdhury, R. Oord, P. Paalanen, B. M. Weckhuysen, *Faraday Discuss*. 2016, **188**, 369–386.

33 B. Hees, L. Puppe, G. Reiss G, *Binder-free molecular sieve zeolite granules which contain zeolites of the type lithium zeolite A and lithium zeolite X*, US 5962358, 1999.

34 F. Akhtar, Q. Liu, N. Hedin and L. Bergström, *Energy Environ. Sci*. 2012, ***5***, 7664–7673.

35 T. Shoinkhorova, A. Dikhtiarenko, A. Ramirez, A. Dutta Chowdhury, M. Caglayan, J. Vittenet, A. Bendjeriou-Sedjerari, O. S. Ali, I. Morales-Osorio, W. Xu, J. Gascon, *ACS Appl. Mater. Interfaces* 2019, **11**, 44133–44143.

36 P. Vasiliev, F. Akhtar, J. Grins, J. Mouzon, C. Andersson, J. Hedlund and L. Bergström, *ACS Appl. Mater. Interfaces* 2010, **2**, 732–737.

37 P. O. Vasiliev, Z. Shen, R. P. Hodgkins, L. Bergström, *Chem. Mater*. 2006, **18**, 4933–4938.

38 F. Akhtar, P. O. Vasiliev, L. Bergström, *J. Am. Ceram. Soc*. 2009, **92**, 338–343.

39 A. K. Nikumbh, P. v. Adhyapak, *Nat. Sci.* 2010, **2**, 694–706.

40 Z. G. Gu, S. C. Chen, W. Q. Fu, Q. Zheng, J. Zhang, *ACS Appl. Mater. Interfaces* 2017, **9**, 7259–7264.

41 Y. Hu, X. Dong, J. Nan, W. Jin, X. Ren, N. Xu, Y. M. Lee, *Chem. Comm*. 2010, **47**, 737–739.

42 L. Sarango, L. Paseta, M. Navarro, B. Zornoza, J. Coronas, *J. Ind. Eng. Chem*. 2018, **59**, 8–16.

43 C. Y. Chaparro-Garnica, P. Jordá-Faus, E. Bailón-García, R. Ocampo-Pérez, C. G. Aguilar-Madera, A. Davó-Quiñonero, D. Lozano-Castelló, A. Bueno-López, *ACS Appl. Mater. Interfaces* 2020, **12**, 54573–54584.

44 E. Peng, D. Zhang, J. Ding, *Adv. Mater*. 2018, **30**, 1802404.

45 A. Shahzad, I. Lazoglu, *Compos. B: Eng*. 2021, **225**, 109249.

46 S. Couck, J. Cousin-Saint-Remi, S. van der Perre, G. v. Baron, C. Minas, P. Ruch, J. F. M. Denayer, *Micropor. Mesopor. Mat*. 2018, **255**, 185–191.

47 H. Thakkar, S. Eastman, Q. Al-Naddaf, A. A. Rownaghi, F. Rezaei, *ACS Appl. Mater. Interfaces* 2017, **9**, 35908–35916.

48 M. J. Regufe, A. F. P. Ferreira, J. M. Loureiro, A. Rodrigues, A. M. Ribeiro, *Microporous Mesoporous Mater*. 2019, **278**, 403–413.

49 D. Popescu, A. Zapciu, C. Amza, F. Baciu, R. Marinescu, *Polym. Test* 2018, **69**, 157–166.

50 P. Dudek, *Arch. Metall. Mater*. 2013, **58**, 1415–1418.

51 J. C. Camargo, Á. R. Machado, E. C. Almeida, E. F. M. S. Silva, *Int. J. Adv. Manuf. Technol*. 2019, **103**, 2423–2443.

52 F. Ning, W. Cong, J. Qiu, J. Wei, S. Wang, *Compos. B: Eng*. 2015, **80**, 369–378.

53 Q. He, J. Jiang, X. Yang, L. Zhang, Z. Zhou, Y. Zhong, Z. Shen, *J. Eur. Ceram. Soc*. 2021, **41**, 1033–1040.

54 N. Mostafa, H. M. Syed, S. Igor, G. Andrew, *Tsinghua Sci. Technol*. 2009, **14**, 29–37.

55 E. R. Kearns, R. Gillespie, D. M. D’Alessandro, *J. Mater. Chem*. A 2021, **9**, 27252–27270.

56 K. Zeng, D. Pal, B. Stucker, in *2012 International Solid Freeform Fabrication Symposium*, University of Texas at Austin, 2012.

57 K. Wudy, M. Hinze, F. Ranft, D. Drummer, W. Schwieger, *J. Mater. Process Technol*. 2017, **246**, 136–143.

58 E. Lahtinen, R. L. M. Precker, M. Lahtinen, E. Hey-Hawkins, M. Haukka, *ChemPlusChem*, 2019, **84**, 222–225.

59 B. Chen, R. Davies, H. Chang, Y. Xia, Y. Zhu, O. Ghita, *Addit. Manuf*. 2021, **38**, 101774.

60 Washington, DC: U.S. Patent and Trademark Office, U.S. Patent No 4,575,330, 1986.

61 X. Wang, M. Jiang, Z. Zhou, J. Gou, D. Hui, *Compos. B: Eng*. 2017, **110**, 442–458.

62 M. L. Griffith, J. W. Halloran, *J. Am. Ceram. Soc*. 2005, **79**, 2601–2608.

63 Z. Chen, Z. Li, J. Li, C. Liu, C. Lao, Y. Fu, C. Liu, Y. Li, P. Wang, Y. He, *J. Eur. Ceram. Soc*. 2019, **39**, 661–687.

64 H. Schulz, P. Burtscher, L. Mädler, *Compos. A: Appl. Sci. Manuf*. 2007, **38**, 2451–2459.

65 T. Nakamoto, K. Yamaguchi, In *MHS'96 Proceedings of the International Symposium on Micro Machine and Human Science*, 1996, 53–58.

66 A. Bertsch, S. Zissi, J. Y. Jézéquel, S. Corbel, J. C. André, *Microsystem. Technologies* 1997, **3**, 42–47.

67 C. Sun, N. Fang, D. M. Wu, X. Zhang, *Sens. Actuators. A: Phys*. 2005, **121**, 113–120.

68 G. W. Hadipoespito, Y. Yang, H. Choi, G. Ning, X. Li, in *2002 International Solid Freeform Fabrication Symposium*, 2003.

69 D. Dudley, W. M. Duncan, J. Slaughter, *In MOEMS display and imaging systems*, SPIE, 2003, **4985**, 14–25.

70 E. M. Maines, M. K. Porwal, C. J. Ellison, T. M. Reineke, *Green Chem*. 2021, **23**, 6863–6897.

71 R. Ding, Y. Du, R. B. Goncalves, L. F. Francis, T. M. Reineke, *Polym. Chem*. 2019, **10**, 1067–1077.

72 Y. Jian, Y. He, T. Jiang, C. Li, W. Yang, J. Nie, *J. Polym. Sci. B: Polym. Phys*. 2012, **50**, 923–928.

73 L. U. Kim, J. W. Kim, C. K. Kim, *Biomacromolecules* 2006, **7**, 2680–2687.

74 F. Montefusco, R. Bongiovanni, M. Sangermano, A. Priola, A. Harden, N. Rehnberg, *Polym.* 2004, **45**, 4663–4668.

75 S. C. Ligon, R. Liska, J. Stampfl, M. Gurr, R. Mülhaupt, *Chem. Rev*. 2017, **117**, 10212–10290.

76 O. Santoliquido, P. Colombo, A. Ortona, *J. Eur. Ceram. Soc*. 2019, **39**, 2140–2148.

77 F. Magzoub, X. Li, S. Lawson, F. Rezaei, A. A. Rownaghi, *Fuel* 2020, **280**, 118628.

78 H. Thakkar, S. Eastman, A. Hajari, A. A. Rownaghi, J. C. Knox, F. Rezaei, *ACS Appl. Mater. Interfaces* 2016, **8**, 27753–27761.

79 J. Knox, R. Gostowski, D. Watson, J. Hogan, E. King, J. Thomas, in *42nd International Conference on Environmental Systems*, American Institute of Aeronautics and Astronautics, Reston, Virigina, 2012, p. 3642.

80 R. Pei, L. Fan, F. Zhao, J. Xiao, Y. Yang, A. Lai, S. F. Zhou, G. Zhan, *J. Hazard. Mater*. 2020, **384**, 121418.

81 K. A. Evans, Z. C. Kennedy, B. W. Arey, J. F. Christ, H. T. Schaef, S. K. Nune, R. L. Erikson, *ACS Appl. Mater. Interfaces* 2018, **10**, 15112–15121.

82 S. Lawson, M. Snarzyk, D. Hanify, A. A. Rownaghi, F. Rezaei, *Ind. Eng. Chem. Res*. 2020, **59**, 7151–7160.

83 J. Dhainaut, M. Bonneau, R. Ueoka, K. Kanamori, S. Furukawa, *ACS Appl. Mater. Interfaces* 2020, **12**, 10983–10992.

84 B. Claessens, N. Dubois, J. Lefevere, S. Mullens, J. Cousin-Saint-Remi, J. F. M. Denayer, *Ind. Eng. Chem. Res*. 2020, **59**, 8813–8824.

85 X. Liu, G. J. H. Lim, Y. Wang, L. Zhang, D. Mullangi, Y. Wu, D. Zhao, J. Ding, A. K. Cheetham, J. Wang, *Chem. Eng. J*. 2021, **403**, 126333.

86 H. Thakkar, S. Lawson, A. A. Rownaghi, F. Rezaei, *Chem. Eng. J.* 2018, **348**, 109–116.

87 S. Wang, P. Bai, M. Sun, W. Liu, D. Li, W. Wu, W. Yan, J. Shang, J. Yu, *Adv. Sci*. 2019, **6**, 1901317.

88 S. Couck, J. Lefevere, S. Mullens, L. Protasova, V. Meynen, G. Desmet, G. v. Baron, J. F. M. Denayer, *Chem. Eng. J*. 2017, **308**, 719–726.

89 H. Thakkar, S. Eastman, A. Al-Mamoori, A. Hajari, A. A. Rownaghi, F. Rezaei, *ACS Appl. Mater. Interfaces* 2017, **9**, 7489–7498.

90 X. Li, W. Li, F. Rezaei, A. Rownaghi, *Chem. Eng. J*. 2018, **333**, 545–553.

91 J. Lefevere, L. Protasova, S. Mullens, V. Meynen, *Mater. Des.* 2017, **134**, 331–341.

92 J. Lefevere, S. Mullens, V. Meynen, *Chem. Eng. J*. 2018, **349**, 260–268.

93 X. Li, F. Rezaei, A. A. Rownaghi, *Microporous Mesoporous Mater*. 2019, **276**, 1–12.

94 F. Magzoub, X. Li, J. Al-Darwish, F. Rezaei, A. A. Rownaghi, *Appl. Catal. B* 2019, **245**, 486–495.

95 S. Lawson, A. Farsad, F. Rezaei, D. Ludlow, A. A. Rownaghi, *ACS Appl. Mater. Interfaces*, 2021, **13**, 781–794.

96 W. Aslam, M. H. Ahmed, T. Qui, M. Konarova, *Chem. Eng. J. Adv*. 2020, **3**, 100024.

97 J. Azuaje, C. R. Tubío, L. Escalante, M. Gómez, F. Guitián, A. Coelho, O. Caamaño, A. Gil, E. Sotelo, *Appl. Catal. A: Gen*. 2017, **530**, 203–210.

98 X. Zhou, C. Liu, *Catal. Today* 2020, **347**, 2–9.

99 A. Quintanilla, J. A. Casas, P. Miranzo, M. I. Osendi, M. Belmonte, *Appl. Catal. B* 2018, **235**, 246–255.

100 M. Areir, Y. Xu, D. Harrison, J. Fyson, *Mater. Sci. Eng. B: Solid State Mater. Adv. Technol*. 2017, **226**, 29–38.

101 M. Areir, Y. Xu, R. Zhang, D. Harrison, J. Fyson, E. Pei, *J. Manuf. Process* 2017, **25**, 351–356.

102 A. Tanwilaisiri, Y. Xu, R. Zhang, D. Harrison, J. Fyson, M. Areir*, J. Energy Storage* 2018, **16**, 1-7.

103 Z. Lyu, G. J. H. Lim, R. Guo, Z. Kou, T. Wang, C. Guan, J. Ding, W. Chen, J. Wang, *Adv. Funct. Mater*. 2019, **29**, 1806658.

104 L. Wang, W. Gao, S. Ng, M. Pumera, *Anal. Chem*. 2021, **93**, 5277–5283.

105 C. Zhu, T. Liu, F. Qian, T. Y. J. Han, E. B. Duoss, J. D. Kuntz, C. M. Spadaccini, M. A. Worsley, Y. Li, *Nano Lett*. 2016, **16**, 3448–3456.

106 A. E. Jakus, E. B. Secor, A. L. Rutz, S. W. Jordan, M. C. Hersam, R. N. Shah, *ACS Nano*, 2015, **9**, 4636–4648.

107 E. García-Tuñon, S. Barg, J. Franco, R. Bell, S. Eslava, E. D'Elia, R. C. Maher, F. Guitian, E. Saiz, *Adv. Mater.* 2015, **27**, 1688–1693.

108 G. de La Osa, D. Pérez-Coll, P. Miranzo, M. I. Osendi, M. Belmonte, *Chem. Mater*. 2016, **28**, 6321–6328.

109 K. Huang, J. Yang, S. Dong, Q. Feng, X. Zhang, Y. Ding, J. Hu, *Carbon* 2018, **130**, 1–10.

110 G. Postiglione, G. Natale, G. Griffini, M. Levi, S. Turri, *Compos. A: Appl. Sci. Manuf*. 2015, **76**, 110–114.

111 B. Chen, Y. Jiang, X. Tang, Y. Pan, S. Hu, *ACS Appl. Mater. Interfaces* 2017, **9**, 28433–28440.

112 G. Sun, J. An, C. K. Chua, H. Pang, J. Zhang, P. Chen, *Electrochem. Commun*. 2015, **51**, 33–36.

113 W. Yu, H. Zhou, B. Q. Li, S. Ding, *ACS Appl. Mater. Interfaces* 2017, **9**, 4597–4604.

114 C. Y. Foo, H. N. Lim, M. A. Mahdi, M. H. Wahid, N. M. Huang, *Sci. Rep*. 2018, **8**, 1–11.

115 C. W. Foster, M. P. Down, Y. Zhang, X. Ji, S. J. Rowley-Neale, G. C. Smith, P. J. Kelly, C. E. Banks, *Sci. Rep.* 2017, **7**, 1–11.

116 S. D. Lacey, D. J. Kirsch, Y. Li, J. T. Morgenstern, B. C. Zarket, Y. Yao, J. Dai, L. Q. Garcia, B. Liu, T. Gao, S. Xu, S. R. Raghavan, J. W. Connell, Y. Lin, L. Hu, *Adv. Mater*. 2018, **30**, 1705651.

117 X. Wei, D. Li, W. Jiang, Z. Gu, X. Wang, Z. Zhang, Z. Sun, *Sci. Rep.* 2015, **5**, 1–7.

118 O. Halevi, T. Y. Chen, P. S. Lee, S. Magdassi, J. A. Hriljac, *RSC Adv.* 2020, **10**, 5766–5776.

119 N. Merilaita, T. Vastamäki, A. Ismailov, E. Levänen, M. Järveläinen, *Ceram. Int*. 2021, **47**, 10742–10748.

120 Y. Zhang, Y. Gao, L. Josien, H. Nouali, C. Vaulot, A. Simon-Masseron, J. Lalevee, *Adv. Mater. Technol*. 2022, **7**, 2100869.

121 Y. Zhang, Y. Gao, L. Michelin, L. Josien, L. Vidal, G. Schrodj, A. Simon-Masseron, J. Lalevée, *Eur. Polym. J*. 2022, **179**, 111552.

122 Y. Gao, Y. Zhang, L. Michelin, J. Lalevée, A. Simon-Masseron, *Mater. Chem. Phys*. 2023, **293**, 126853.

123 A. J. Young, R. Guillet-Nicolas, E. S. Marshall, F. Kleitz, A. J. Goodhand, L. B. L. Glanville, M. R. Reithofer, J. M. Chin, *Chem. Commun*. 2019, **55**, 2190–2193.

124 O. Halevi, J. M. R. Tan, P. S. Lee, S. Magdassi, *Adv. Sustain. Syst*. 2018, **2**, 1700150.

125 A. C. Shortcill, W. M. Palin, P. Burtscher, *J. Dent. Res*. 2008, **87**, 84–88.

126 M. Kawaguchi, T. Fukushima, K. Miyazaki, *J. Dent. Res*. 1994, **73**, 516–521.

127 O. Halevi, J. Chen, G. Thangavel, S. A. Morris, T. ben Uliel, Y. R. Tischler, P. S. Lee, S. Magdassi, *RSC Adv*. 2020, **10**, 14812.

128 J. Y. Huang, H. Xu, E. Peretz, D. Y. Wu, C. K. Ober, T. Hanrath, *Chem. Mater*. 2019, **31**, 10017–10022.

129 Z. Hu, Y. Wang, B. B. Shah, D. Zhao, *Adv. Sustain. Syst*. 2019, **3**, 1800080.

130 E. Shukrun Farrell, Y. Schilt, M. Y. Moshkovitz, Y. Levi-Kalisman, U. Raviv, S. Magdassi, *Nano Lett*. 2020, **20**, 6598–6605.

131 H. Zhang, P. Wang, H. Zhang, H. Yang, H. Wang, L. Zhang, *Ind. Eng. Chem. Res*. 2020, **59**, 8223–8229.

132 L. Sa, L. Kaiwu, C. Shenggui, Y. Junzhong, J. Yongguang, W. Lin, R. Li, *J. Mater. Sci*. 2019, **54**, 3309–3318.

133 R. Li, S. Yuan, W. Zhang, H. Zheng, W. Zhu, B. Li, M. Zhou, A. Wing-Keung Law, K. Zhou, *ACS Appl. Mater. Interfaces* 2019, **11**, 40564–40574.

134 A. Azhari, E. Marzbanrad, D. Yilman, E. Toyserkani, M. A. Pope, *Carbon* 2017, **119**, 257–266.

135 S. Lawson, X. Li, H. Thakkar, A. A. Rownaghi, F. Rezaei, *Chem. Rev.* 2021, **121**, 6246–6291.

136 J. Zhou, X. Allonas, A. Ibrahim, X. Liu, Prog. *Polym. Sci.* 2019, **99**, 101165.

137 X. Shen, M. Chu, F. Hariri, G. Vedula, H.E. Naguib, *Addit. Manuf.* 2020, **36**, 101565.